Supporting Information

Back donation, intramolecular electron transfer and N-O bond scission targeting nitrogen oxyanion reduction: how can a metal complex assist?

Table of contents

Computational details.

General details. DFT[1] calculations were carried out using Gaussian 16.[2] Geometry optimizations were performed at the B3LYP-D3BJ/6-311G(d) level of theory.[3-5] All optimized structures were visualized using GaussView 6[6] and were confirmed to be minima by analyzing the harmonic frequencies.[7,8] The SDD effective core potentials was used for Ru and Rh.[9] Several single point energy calculations were performed using the implicit SMD[10] model to account for solvent effects using benzene, THF, or acetonitrile. Downloadable .mol files are available for each optimized structure

1. Parr, R.G.; Yang, W. Density-functional theory of atoms and molecules; Oxford University Press: New York, 1989.
2. Gaussian 16, Revision C.01, Frisch, M. J.; Trucks, G. W.; Schlegel, H. B.; Scuseria, G. E.; Robb, M. A.; Cheeseman, J. R.; Scalmani, G.; Barone, V.; Petersson, G. A.; Nakatsuji, H.; Li, X.; Caricato, M.; Marenich, A. V.; Bloino, J.; Janesko, B. G.; Gomperts, R.; Mennucci, B.; Hratchian, H. P.; Ortiz, J. V.; Izmaylov, A. F.; Sonnenberg, J. L.; Williams-Young, D.; Ding, F.; Lipparini, F.; Egidi, F.; Goings, J.; Peng, B.; Petrone, A.; Henderson, T.; Ranasinghe, D.; Zakrzewski, V. G.; Gao, J.; Rega, N.; Zheng, G.; Liang, W.; Hada, M.; Ehara, M.; Toyota, K.; Fukuda, R.; Hasegawa, J.; Ishida, M.; Nakajima, T.; Honda, Y.; Kitao, O.; Nakai, H.; Vreven, T.; Throssell, K.; Montgomery, J. A., Jr.; Peralta, J. E.; Ogliaro, F.; Bearpark, M. J.; Heyd, J. J.; Brothers, E. N.; Kudin, K. N.; Staroverov, V. N.; Keith, T. A.; Kobayashi, R.; Normand, J.; Raghavachari, K.; Rendell, A. P.; Burant, J. C.; Iyengar, S. S.; Tomasi, J.; Cossi, M.; Millam, J. M.; Klene, M.; Adamo, C.; Cammi, R.; Ochterski, J. W.; Martin, R. L.; Morokuma, K.; Farkas, O.; Foresman, J. B.; Fox, D. J. Gaussian, Inc., Wallingford CT, 2016.
3. (a) Vosko, S. H.; Wilk, L.; Nusair, M. *Can. J. Phys.* **1980**, *58*, 1200. (b) Lee, C.; Yang, W.; Parr, R.G. *Phys. Rev. B* **1988**, *37*, 785. (c) Becke, A. D. *J. Chem. Phys.* **1993**, *98*, 5648. (d) Stephens, P.J.; Devlin, F. J.; Chabalowski, C. F.; Frisch, M.J. *J. Phys. Chem.* **1994**, *98*, 11623.
4. Grimme, S.; Antony, J.; Ehrlich, S.; Krieg, H., *J. Chem. Phys.*, **2010,** *132,* 154104.
5. Grimme, S.; Ehrlich, S.; Goerigk, L.; *J. Comput. Chem.,* **2010***, 32,* 1456.
6. GaussView, Version 6, Dennington, Roy; Keith, Todd A.; Millam, John M. Semichem Inc., Shawnee Mission, KS, 2016.
7. (a) Schlegel, H. B.; McDouall, J. J. in Computational Advances in Organic Chemistry; Oeretir, C; Csizmadia, I. G., Eds.; Kluwer Academic: Amsterdam, The Netherlands, 1991. (b) Bauernschmitt, R.; Ahlrichs, R. *J. Chem. Phys.* **1996**, *104*, 9047.
8. Schlegel, H. B. *WIREs Comput. Mol. Sci.* **2011**, *1*, 790.
9. Dolg, M.; Wedig, U.; Stoll, H.; Preuss, H. J. *J. Chem. Phys*. **1987**, *86*, 866.
10. Marenich, A. V.; Cramer, C. J.; Truhlar, D. G., *J. Phys. Chem. B*, **2009**, *113*, 6378.

Discussion of $[CpRu(PMe_3)(L)(X)]^{0/-}$ calculations.

General description of this class of compounds.

We initially chose to study this suite of compounds to avoid the possibility of multiple spin states, along with the fact that these compounds are saturated, 18 valence electron species. We considered a variety of X-type ligands with CO and pyridine as neutral L type donors.

Neutral $CpRu(PMe_3)(CO)(X)$.

For these molecules, the calculated CO and relevant NO_x vibrational frequencies (Table S1) show the nitrate complex has the highest CO stretching frequency. While this might be interpreted as the nitrate being a strong π acid, competing well against CO, this ignores variation

of σ donor ability among X. For example because the ν_{CO} for X = CH_3 and BMe_2 differ by only 5 cm^{-1}, the better BMe_2 σ-donation (decreased electronegativity at B vs. C) is offset by the π-acidity of BMe_2. Additionally, X = BF_2 gives a ν_{CO} 27 cm^{-1} higher than X = BMe_2, but this may be attributed to the weaker σ-donating effect of BF_2 compared to BMe_2. Because BF_2^- and NO_2^- are isoelectronic, both 18 valence electrons (although nitrogen has the higher formal oxidation state), comparative calculations can reveal whether any back donation occurs to BF_2 by 1) its changed BF and MB bond lengths on reduction and 2) its two BF stretching frequencies. There are only minor bond length changes upon reduction (Figure S9), and the coupling of BF stretching frequencies to ancillary ligand motions (Cp C-H stretch) makes arguments about back donation based on stretching frequencies difficult. In the calculations reported here, the CO frequency is 23 – 27 cm^{-1} higher for BF_2 than for BMe_2, showing that diminished π acidity of BF_2 is not the major feature, and that its diminished σ donation must dominate.

Table S1. Calculated IR stretching frequencies for $CpRu(PMe_3)(CO)(X)$. For nitrite species, NO_2 notation indicates nitrite and ONO notation indicates nitrito

Complex	CO stretch (cm^{-1})	NO_x^- stretch (cm^{-1})
$CpRu(PMe_3)(CO)(H)$	1939	—
$CpRu(PMe_3)(CO)(CH_3)$	1934	—
$CpRu(PMe_3)(CO)(ONO_2)$	1991	1527, 1253
$CpRu(PMe_3)(CO)(NO_2)$	1984	1436, 1315
$CpRu(PMe_3)(CO)(ONO)$	1980	1437, 1084
$CpRu(PMe_3)(CO)(BMe_2)$	1929	—
$CpRu(PMe_3)(CO)(BF_2)$	1956	—

The ν_{CO} trend among NO_2, ONO and nitrate is confusing. Any OR ligand attached to a 17 electron fragment is subject to lone pair/filled dπ orbital repulsions (filled/filled repulsion) which lengthens the M-O bond and diminishes the more distance-sensitive π overlap. In that sense, the O in both $O(NO_x)$ is a more insulating connector between M and N. The two O donor ligands nitrate and nitrito have two lone pairs on the donor atom *vs.* none for NO_2. Given that variable σ donor and π acceptor strength contribute to the overall changes in ν_{CO}, we chose OH as a control for donation by an OE-ligand with no π acceptor capacity in E. We thus compare MOR where R = H^+, NO_2^+, and NO^+, as three different electrophiles operating on the electronic character of the oxo group. For $CpRu(CO)(PMe_3)(OH)$, the low ν_{CO} value, 1941 cm^{-1}, shows that the combination of its σ donor and π/π repulsion nearly equals the donor power of the pure σ ligands H and CH_3; this shows ONO and ONO_2 to be much weaker donors than the useful comparison standard, OH. The high ν_{CO} for X = NO_2 is due to its high π acidity.

Neutral $CpRu(PMe_3)(py)(X)$.

To further address this "two changing variables" problem, we compared (Table S2) the three NO_x against a systematically altered $CpRu(PMe_3)L$ π base; Ru was anticipated be more π basic for L = pyridine than for L = CO, as reflected in NO stretching frequencies. We compare only the higher NO frequency for each because the lower frequencies show, by inspection of animations, mixing with other atom motions (e.g. HCH scissoring). Judged by Δ in Table S2, NO_2 shows the strongest evidence for π acidity, and nitrato and nitrito little and none.

Table S2. Comparison of higher energy NO_x^- stretches in $CpRu(PMe_3)_2(L)(X)$ between L = pyr and CO.

Complex	NO_x^- stretch (cm^{-1}), L = py	NO_x^- stretch (cm^{-1}), L = CO	$\Delta = \nu(py) - \nu(CO)$
$CpRu(PMe_3)(L)(ONO_2)$	1517	1527	-10

$CpRu(PMe_3)(L)(NO_2)$	1390	1436	-46
$CpRu(PMe_3)(L)(ONO)$	1438	1437	+1

One electron reduced $[CpRu(PMe_3)(L)(X)]^-$.

In order to further probe the π-acidity of nitrate, each calculation presented above was also done with an anionic charge, where spin densities in these radicals supplement stretching frequencies to reveal the extent of delocalization of the added electron. A comparative list of relevant stretching frequencies is detailed in Table S3. Likewise, a comparative list of relavent stretching frequencies for the pyridine analogues is detailed in Table S4. In Table S4, the $[CpRu(PMe_3)(py)(ONO)]^{0/-}$ comparison is not made, because the reduced species shows evidence of nitrite dissociation (Figure S6).

Table S3. calculated stretching frequencies for $[CpRu(PMe_3)(CO)(X)]^-$. $[CpRu(CO)(PMe_3)(ONO_2)]^-$ is omitted, as an optimized structure was never found. The CO stretches for the neutral species are shown in Table S1.

Complex	ν_{CO} (cm^{-1})	Δ(CO), anion - neutral	ν_{NO} (cm^{-1})	Δ(NO), anion - neutral
$[CpRu(CO)(PMe_3)(H)]^-$	1813	-126	—	—
$[CpRu(CO)(PMe_3)(CH_3)]^-$	1805	-129	—	—
$[CpRu(CO)(PMe_3)(NO_2)]^-$	1807	-177	1371	-65
$[CpRu(CO)(PMe_3)(ONO)]^-$	1864	-116	1323	-114
$[CpRu(CO)(PMe_3)(BMe_2)]^-$	1817	-112	—	—
$[CpRu(CO)(PMe_3)(BF_2)]^-$	1840	-116	—	—

Table S4. comparison of stretching frequencies for $[CpRu(PMe_3)(py)(X)]^{0/-}$.

Complex	ν_{NO} for neutral	ν_{NO} for anion	Δ, anion-neutral
$[CpRu(PMe_3)(py)(ONO_2)]^{0/-}$	1517	1471	-46
$[CpRu(PMe_3)(py)(NO_2)]^{0/-}$	1390	1349	-41

Addition of one electron significantly lowers every CO stretching frequency (Table S4), consistent with a more electron rich metal center, but comparing $CpRu(CO)(PMe_3)(NO_2)$ and $[CpRu(CO)(PMe_3)(NO_2)]^-$, the larger NO stretching frequency decrease indicates that reduction causes nitro to accept more electron density than any other X; the magnitude of the NO frequency decrease, Δ(NO), is also large. However, the spin density plot of $[CpRu(CO)(PMe_3)(NO_2)]^-$ shows unpaired spin primarily on the metal center *and the carbonyl*. Reduction of CO is also evident in an RuCO angle of 160.6°. Interestingly, the spin density plots of $[CpRu(pyr)(PMe_3)(NO_2)]^-$ also show no spin density on the X-type ligand; instead, the unpaired spin is primarily metal and *pyridine* based. Again, the LUMO of the neutral species is a d-orbital that is orthogonal to the π-system of the X-type ligand, although back donation occurs through doubly occupied orbitals, not merely by appearance of unpaired spin density at the π acid ligand in the radical monoanions.

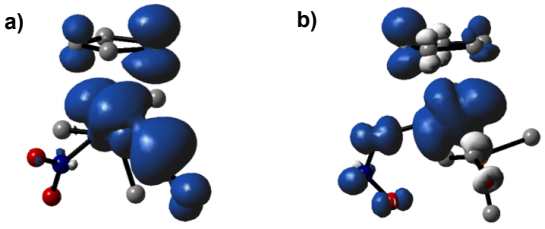

Figure S1. a) Spin density plot (0.002 au) for $[CpRu(PMe_3)(CO)(NO_2)]^-$ **b)** Spin density plot (0.002 au) for $[CpRu(PMe_3)(CO)(ONO)]^-$.

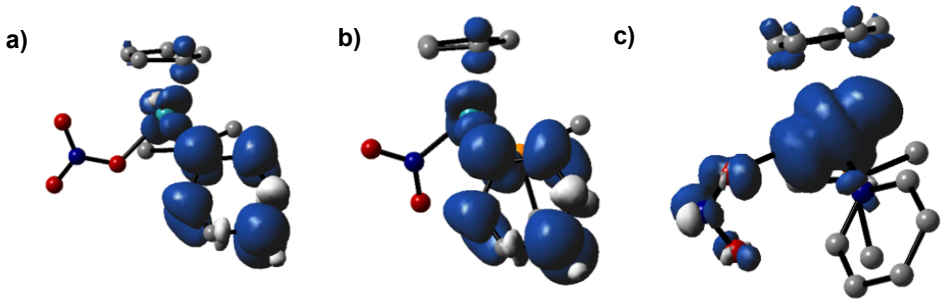

Figure S2. Spin density plots (0.002 au) for **a)** $[CpRu(PMe_3)(pyr)(ONO_2)]^-$ **b)** $[CpRu(PMe_3)(pyr)(NO_2)]^-$ **c)** $[CpRu(PMe_3)(pyr)(ONO)]^-$.

Structural trends for [CpRu(PMe$_3$)(L)(X)].

For a detailed comparison of structural trends within the $[CpRu(PMe_3)(L)(X)]^{0/-}$ series, see figures S3-S16. Notably, the anionic RuNO2 species shows the best evidence for back donation into the X type ligand, consistent with the spectroscopic data. The anionic RuNO2 complex exhibits RuN shortening, NO lengthening, and RuC(O) lengthening (0.03 A); upon reduction it is unique in RuC(O) lengthening. The nitrito and nitrato complexes show evidence, upon reduction, for dissociating the NOx- ion via dramatic lengthening of the RuO distance, suggesting that the 17 valence electron radical $CpRu(PMe_3)(CO)^{\bullet}$ and free nitrogen oxyanions are energetically competitive with their adduct, favoring *metal/oxygen* bond scission. Not only CO, but also pyridine is a strong π acid competitor to NO_x^-. As evidenced by the spin density maps (FigsS?-S?), reduction of $CpRu(PMe_3)(py)X$ is primarily pyridine based. Population of pyridine pi star is more favorable than the formation of a 19 valence electron complex, and there has been experimental evidence for redox activity in M-py complexes. Anionic pyridine is nonplanar, with alternating bond lengths within the ring, and pyramidal at ring nitrogen in all $CpRu(PMe_3)(py)X^{-1\bullet}$. In each *neutral* $CpRu(PMe_3)(L)X$ studied here, the nitro linkage isomer is more stable than the nitrito, by 4 to 12 kcal/mol [We exclude from the comparison the anionic ruthenium nitrito since it undergoes anion dissociation upon reduction]. In every *radical anion*, the nitro is favored even more, which is attributed to the reinforcing factors of back donation to nitro being more important in the electron rich anions and also the filled/filled *repulsion* of an ONO linkage isomer being *increased* upon reduction.

Ancillary ligands CO or pyridine show dominant back donation to the π systems of *both* those ligands. Upon adding one electron, the pyridine CN distances lengthen, becoming more single bond as N becomes amide: the orbital housing the new amide lone pair does NOT donate to Ru, but does show push/pull conjugation on rhodium, most likely due to the square planar geometry of those complexes. When a nitrogen oxyanion lacks ability (LUMO energy) to accept electrons, M/O bond heterolysis is found to be a preferred reaction channel to avoid excess charge buildup, as seen with $[CpRu(PMe_3)(CO)(ONO)]^-$ and $[CpRu(PMe_3)(CO)(ONO_2)]^-$.

All CpRu(PMe3)(CO)X show (see below) CC distances unaltered in anions compared to neutrals, but RuC distances lengthen and become variable in the anions; Ru/ring centroid distances lengthen by ~0.3 Å. Upon reduction, distances to hydride or to methyl change less than 0.01 Å, while distances to B shorten by 0.05- 0.07 Å, and BF distances lengthen. The anionic RuNO2 species is outstanding for RuN shortening, NO lengthening, and RuC(O) longer (by 0.03 Å); upon reduction it is unique in RuC lengthening. While all anions show CO lengthening (by ~0.02 Å, consistent with calculated νCO decrease)), and anions generally show some RuCO bending (~173°): the nitro complex has that angle at 160.6° . In the neutrals, binding to the CpRu(PMe3)(CO) center makes the ON distances different by 0.07 Å for RuONO and 0.09 Å for $RuONO_2$. The nitrito complex shows evidence, upon reduction, for dissociating the ONOion, via dramatic (0.38 Å) lengthening of the RuO distance, and its two NO distances become more

similar; again this suggests that CpRu(PMe3)(CO)• and free nitrite are energetically competitive vs. their adduct. Nitrate shows this effect even more strongly. Nitro is the most perturbing of back donation to CO of the X studied here.

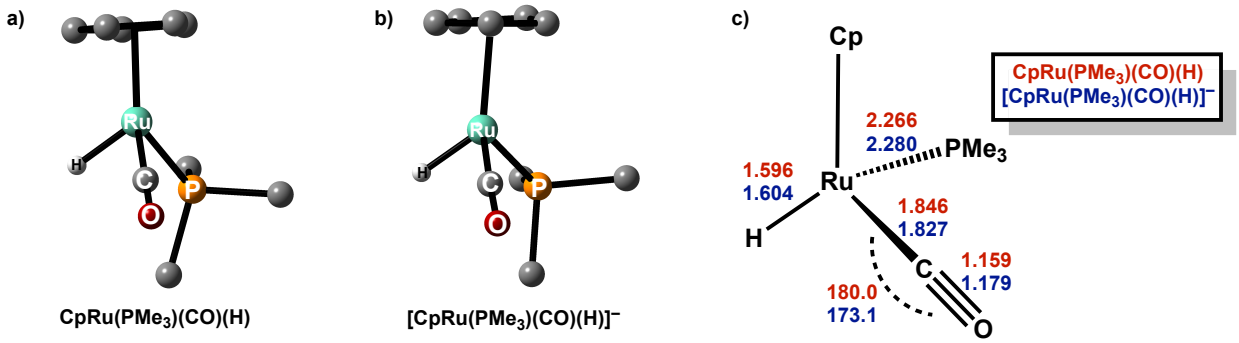

Figure S3. a) geometry optimized structure of $CpRu(PMe_3)(CO)(H)$. Ru–centroid distance is 1.96 Å, all Ru–Cp carbon distances are between 2.29-2.33 Å. C–C bonds within Cp ring are 1.41-1.44 Å. **b)** geometry optimized structure of $[CpRu(PMe_3)(CO)(H)]^-$. Ru–centroid distance is 2.30 Å, all Ru–Cp carbon distances are between 2.40-2.84 Å. C–C bonds within Cp ring are 1.41-1.43 Å. **c)** bond length comparison between $[CpRu(PMe_3)(CO)(H)]^{0/-}$.

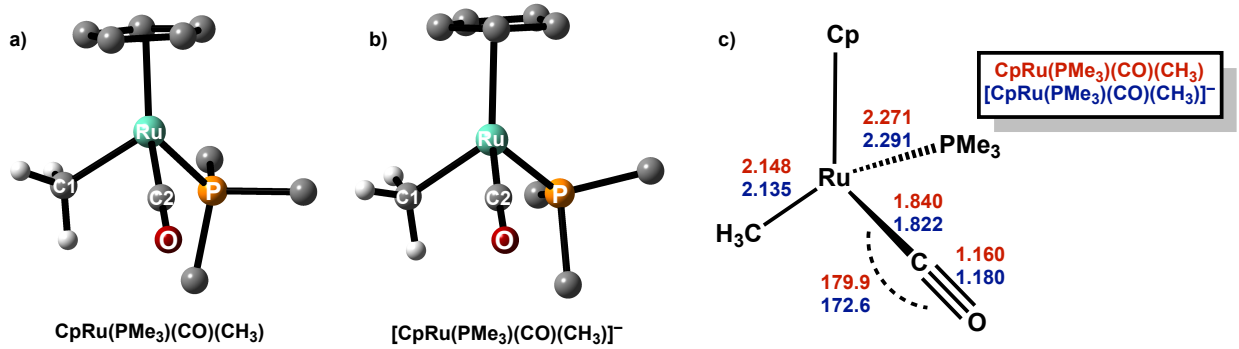

Figure S4. a) geometry optimized structure of $CpRu(PMe_3)(CO)(CH_3)$. Ru–centroid distance is 1.97 Å, all Ru–Cp carbon distances are 2.31 Å. C–C bonds within Cp ring are 1.42-1.44 Å. **b)** geometry optimized structure of $[CpRu(PMe_3)(CO)(CH_3)]^-$. Ru–centroid distance is 2.32 Å, all Ru–Cp carbon distances are between 2.40-2.86 Å. C–C bonds within Cp ring are 1.41-1.43 Å. **c)** bond length comparison between $[CpRu(PMe_3)(CO)(CH_3)]^{0/-}$.

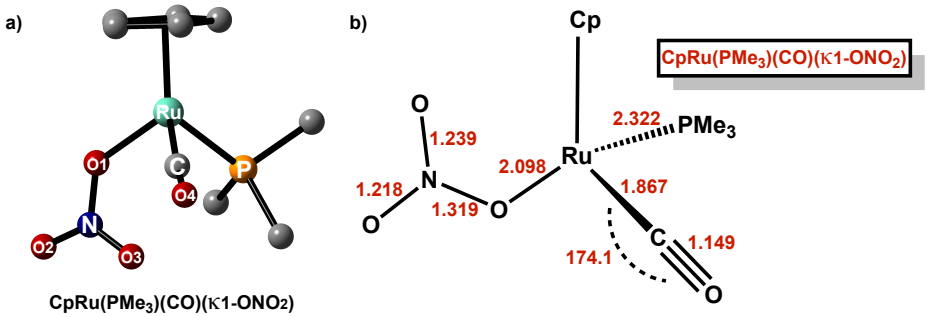

Figure S5. a) geometry optimized structure of $CpRu(PMe_3)(CO)(\kappa^1\text{-}NO_3)$. Ru–centroid distance is 1.92 Å, all Ru–Cp carbon distances are between 2.23-2.30 Å. C–C bonds within Cp ring are 1.42-1.44 Å. **b)** selected bond lengths in $CpRu(PMe_3)(CO)(\kappa^1\text{-}NO_3)$.

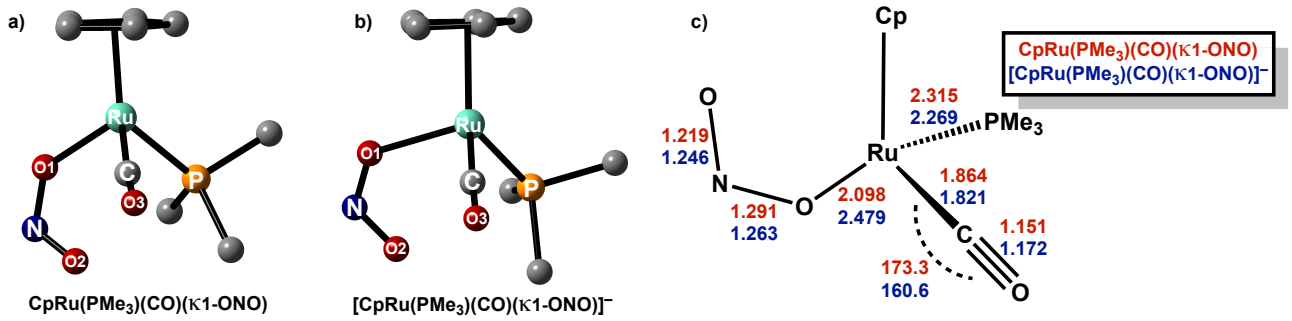

Figure S6. a) geometry optimized structure of $CpRu(PMe_3)(CO)(\kappa^1\text{-}ONO)$. Ru–centroid distance is 1.93 Å, all Ru–Cp carbon distances are between 2.24-2.32 Å. C–C bonds within Cp ring are 1.42-1.44 Å. **b)** geometry optimized structure of $[CpRu(PMe_3)(CO)(\kappa^1\text{-}ONO)]^-$. Ru–centroid distance is 2.14 Å, all Ru–Cp carbon distances are between 2.40-2.54 Å. C–C bonds within Cp ring are 1.41-1.44 Å. **c)** bond length comparison between $[CpRu(PMe_3)(CO)(\kappa^1\text{-}ONO)]^{0/-}$.

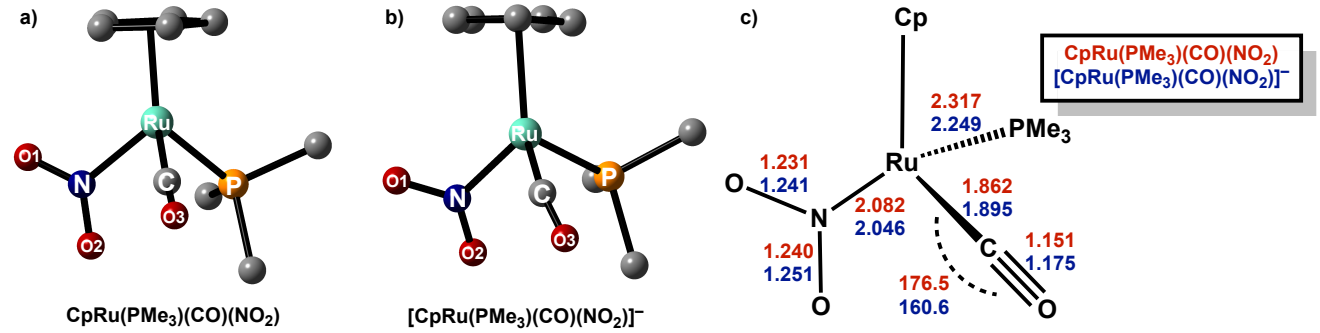

Figure S7. a) geometry optimized structure of $CpRu(PMe_3)(CO)(NO_2)$. Ru–centroid distance is 1.95 Å, all Ru–Cp carbon distances are between 2.28-2.31 Å. C–C bonds within Cp ring are 1.42-1.44 Å. **b)** geometry optimized structure of $[CpRu(PMe_3)(CO)(NO_2)]^-$. Ru–centroid distance is 2.27 Å, all Ru–Cp carbon distances are between 2.39-2.74 Å. C–C bonds within Cp ring are 1.40-1.44 Å. **c)** bond length comparison between $[CpRu(PMe_3)(CO)(NO_2)]^{0/-}$.

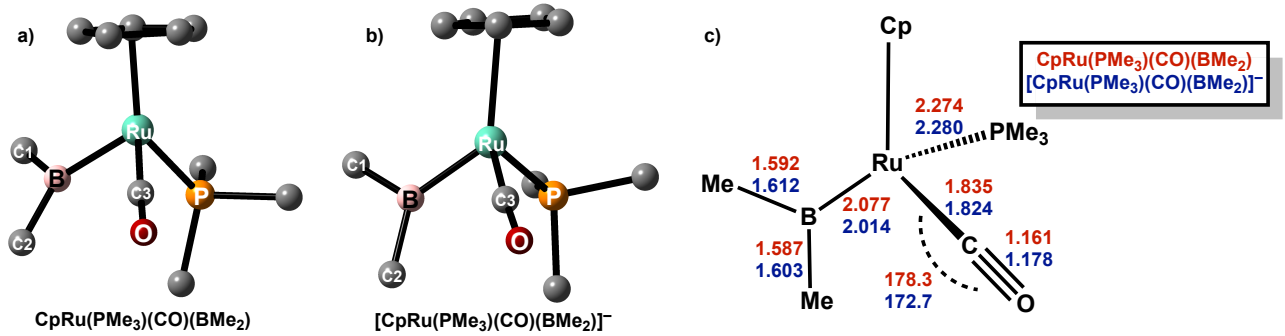

Figure S8. a) geometry optimized structure of $CpRu(PMe_3)(CO)(BMe_2)$. Ru–centroid distance is 2.00 Å, all Ru–Cp carbon distances are between 2.30-2.38 Å. C–C bonds within Cp ring are 1.42-1.44 Å. **b)** geometry optimized structure of $[CpRu(PMe_3)(CO)(BMe_2)]^-$. Ru–centroid distance is 2.42 Å, all Ru–Cp carbon distances are between 2.47-2.98 Å. C–C bonds within Cp ring are 1.41-1.43 Å. **c)** bond length comparison between $[CpRu(PMe_3)(CO)(BMe_2)]^{0/-}$.

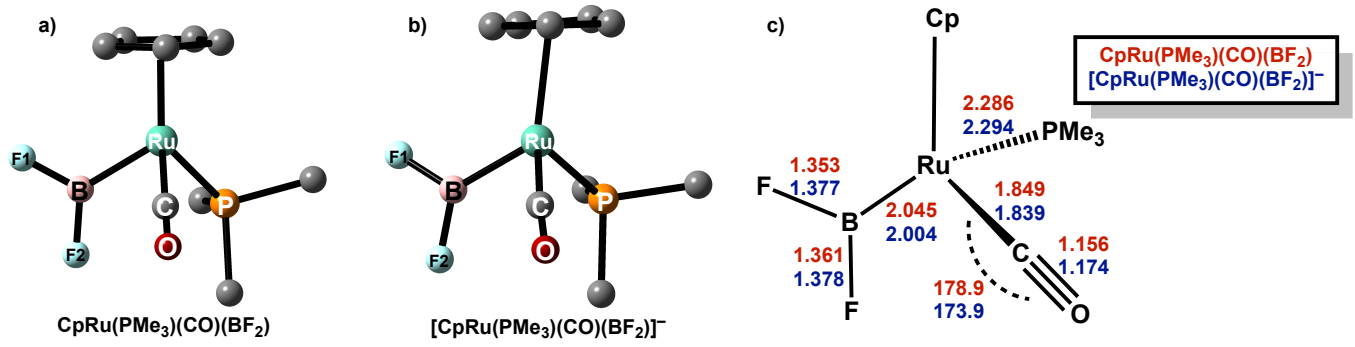

Figure S9. a) geometry optimized structure of $CpRu(PMe_3)(CO)(BF_2)$. Ru–centroid distance is 1.97 Å, all Ru–Cp carbon distances are between 2.29-2.36 Å. C–C bonds within Cp ring are 1.42-1.43 Å. **b)** geometry optimized structure of $[CpRu(PMe_3)(CO)(BF_2)]^-$. Ru–centroid distance is 2.30 Å, all Ru–Cp carbon distances are between 2.40-2.82 Å. C–C bonds within Cp ring are 1.42-1.43 Å. **c)** bond length comparison between $[CpRu(PMe_3)(CO)(BF_2)]^{0/-}$.

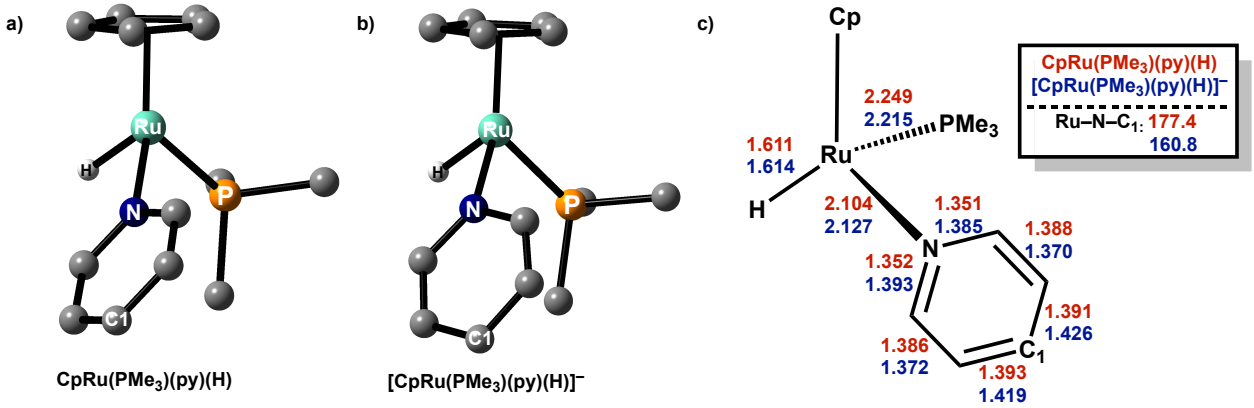

Figure S10. a) geometry optimized structure of $CpRu(PMe_3)(py)(H)$. Ru–centroid distance is 1.91 Å, all Ru–Cp carbon distances are between 2.21-2.33 Å. C–C bonds within Cp ring are 1.42-1.44 Å. **b)** geometry optimized structure of $[CpRu(PMe_3)(py)(H)]^-$. Ru–centroid distance is 1.94 Å, all Ru–Cp carbon distances are between 2.24-2.34 Å. C–C bonds within Cp ring are 1.42-1.44 Å. **c)** bond length comparison between $[CpRu(PMe_3)(py)(H)]^{0/-}$.

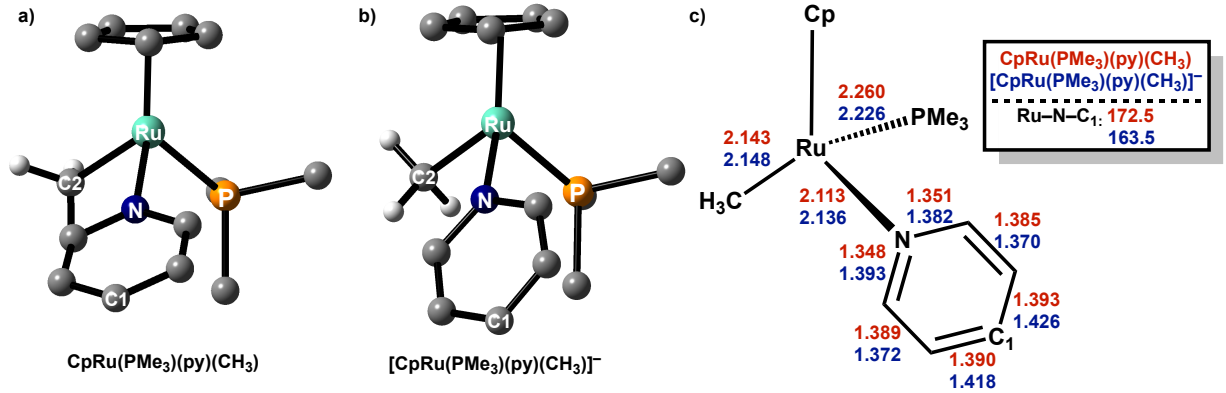

Figure S11. a) geometry optimized structure of $CpRu(PMe_3)(py)(CH_3)$. Ru–centroid distance is 1.91 Å, all Ru–Cp carbon distances are between 2.21-2.31 Å. C–C bonds within Cp ring are 1.41-1.44 Å. **b)** geometry optimized structure of $[CpRu(PMe_3)(py)(CH_3)]^-$. Ru–centroid distance is 1.93 Å, all Ru–Cp carbon distances are between 2.22-2.33 Å. C–C bonds within Cp ring are 1.42-1.44 Å. **c)** bond length comparison between $[CpRu(PMe_3)(py)(CH_3)]^{0/-}$.

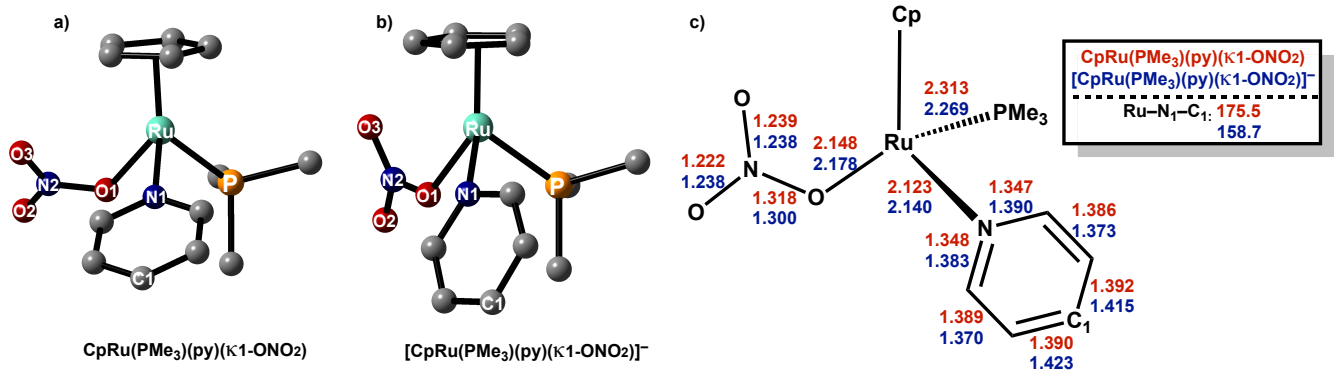

Figure S12. a) geometry optimized structure of $CpRu(PMe_3)(py)(\kappa^1\text{-}ONO_2)$. Ru–centroid distance is 1.85 Å, all Ru–Cp carbon distances are between 2.19-2.24 Å. C–C bonds within Cp ring are 1.42-1.45 Å. **b)** geometry optimized structure of $[CpRu(PMe_3)(py)(\kappa^1\text{-}ONO_2)]^-$. Ru–centroid distance is 1.88 Å, all Ru–Cp carbon distances are between 2.20-2.28 Å. C–C bonds within Cp ring are 1.41-1.45 Å. **c)** bond length comparison between $[CpRu(PMe_3)(py)(\kappa^1\text{-}ONO_2)]^{0/-}$.

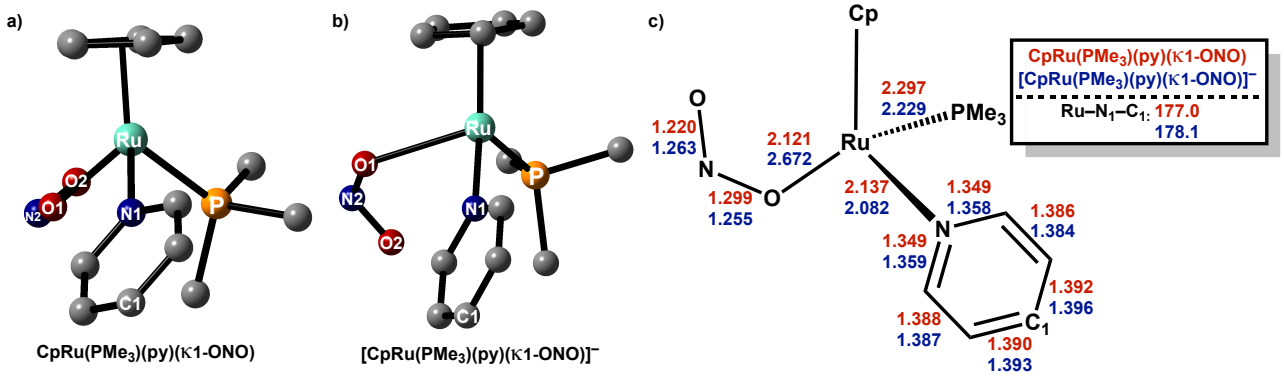

Figure S13. a) geometry optimized structure of $CpRu(PMe_3)(py)(\kappa^1\text{-}ONO)$. Ru–centroid distance is 1.87 Å, all Ru–Cp carbon distances are between 2.21-2.26 Å. C–C bonds within Cp ring are 1.42-1.44 Å. **b)** geometry optimized structure of $[CpRu(PMe_3)(py)(\kappa^1\text{-}ONO)]^-$. Ru–centroid distance is 2.12 Å, all Ru–Cp carbon distances are between 2.32-2.56 Å. C–C bonds within Cp ring are 1.41-1.44 Å. **c)** bond length comparison between $[CpRu(PMe_3)(py)(\kappa^1\text{-}ONO)]^{0/-}$.

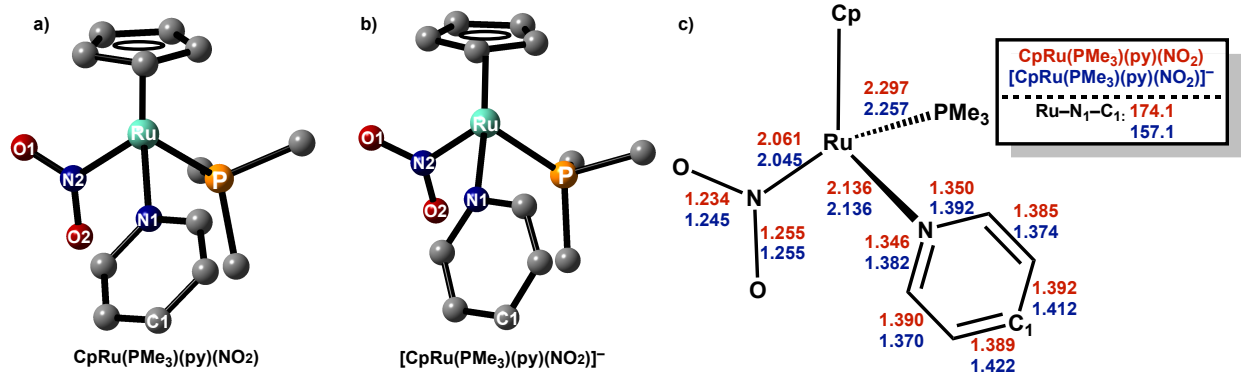

Figure S14 a) geometry optimized structure of $CpRu(PMe_3)(py)(NO_2)$. Ru–centroid distance is 1.90 Å, all Ru–Cp carbon distances are between 2.06-2.28 Å. C–C bonds within Cp ring are 1.42-1.44 Å. **b)** geometry optimized structure of $[CpRu(PMe_3)(py)(NO_2)]^-$. Ru–centroid distance is 1.95 Å, all Ru–Cp carbon distances are between 2.25-2.34 Å. C–C bonds within Cp ring are 1.42-1.44 Å. **c)** bond length comparison between $[CpRu(PMe_3)(py)(NO_2)]^{0/-}$.

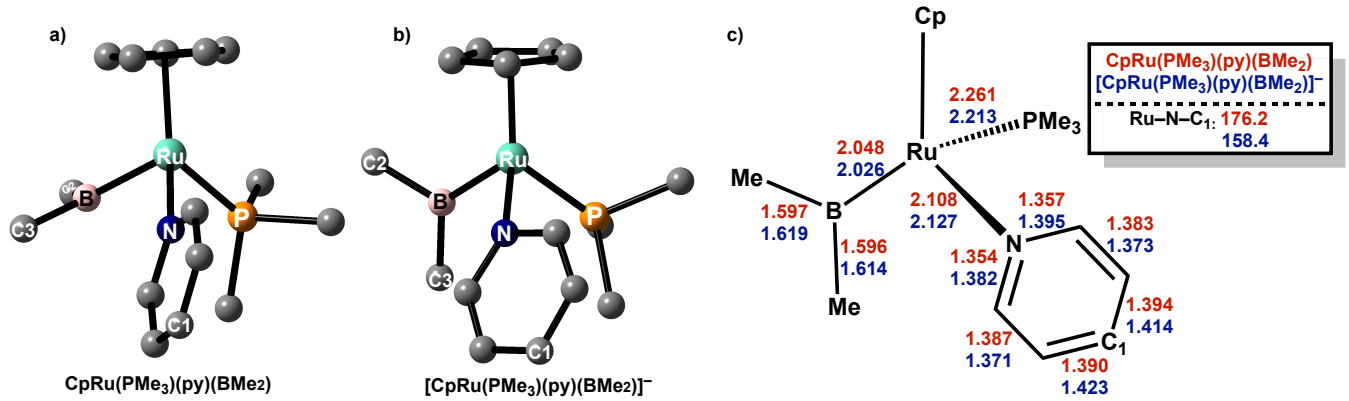

Figure S15. a) geometry optimized structure of $CpRu(PMe_3)(py)(BMe_2)$. Ru–centroid distance is 1.97 Å, all Ru–Cp carbon distances are between 2.26-2.39 Å. C–C bonds within Cp ring are 1.41-1.44 Å. **b)** geometry optimized structure of $[CpRu(PMe_3)(py)(BMe_2)]^-$. Ru–centroid distance is 2.05 Å, all Ru–Cp carbon distances are between 2.29-2.47 Å. C–C bonds within Cp ring are 1.41-1.44 Å. **c)** bond length comparison between $[CpRu(PMe_3)(py)(BMe_2)]^{0/-}$.

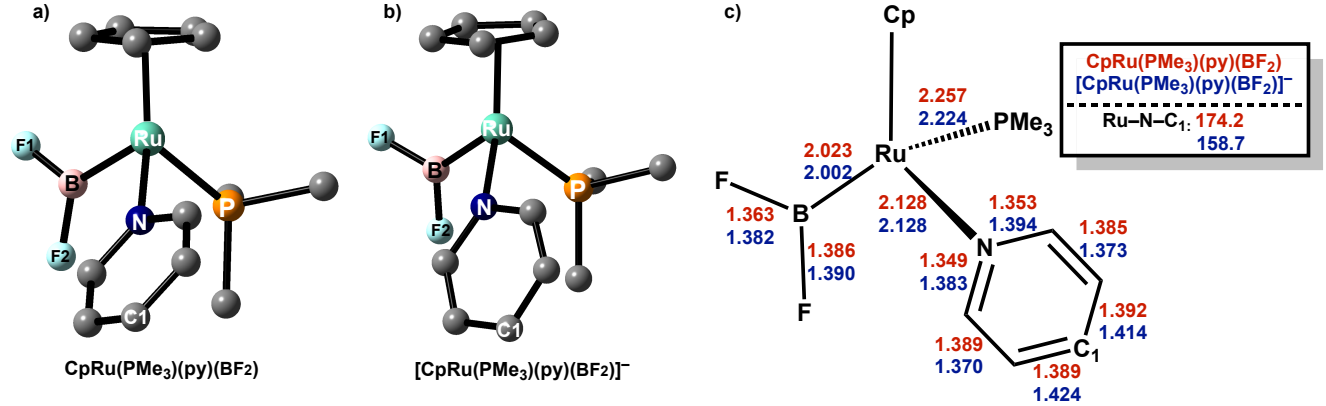

Figure S16. a) geometry optimized structure of $CpRu(PMe_3)(py)(BF_2)$. Ru–centroid distance is 1.95 Å, all Ru–Cp carbon distances are between 2.23-2.37 Å. C–C bonds within Cp ring are 1.42-1.43 Å. **b)** geometry optimized structure of $[CpRu(PMe_3)(py)(BF_2)]^-$. Ru–centroid distance is 2.00 Å, all Ru–Cp carbon distances are between 2.26-2.41 Å. C–C bonds within Cp ring are 1.41-1.44 Å. **c)** bond length comparison between $[CpRu(PMe_3)(py)(BF_2)]^{0/-}$.

$[CpRu(PMe_3)(L)(X)]^{0/-}$ conclusions.

Overall, spin density in the reduced complexes was primarily metal, CO, and pyridine based, and the reduction was accompanied by only small bond length changes within the M-X unit for the majority of the complexes. The stretching frequencies of the nitrogen oxyanions were often coupled to other ancillary ligand motions, making it difficult to gauge back donation simply based on N-O stretching frequencies. The $RuNO_2$ species was the most indicative of any nitrogen oxyanion behaving as a π-acid.

Discussion of $[Rh(PMe_3)_2(CO)(X)]^{0/-}$ calculations.

General description of this class of compounds.

To gauge the effect of geometry and valence electron count on N oxyanion -acidity, we did the analogous calculations with d^8 square planar rhodium(I).

Neutral $Rh(PMe_3)_2(CO)(X)$.

The data in Table S5 reflects the same general X ligand trends as in Table S1. Notably, ν_{CO} for X = H is anomalously high, due to mixing with $\nu_{Rh\text{-}H}$. Both vibrational and *electronic* communication is different here from in the Ru series, due to *trans* location of L and X on Rh. The nitrate example in this case failed to optimize for the neutral species, and is thus omitted in Table S5.

Table S5. Calculated stretching frequencies for $Rh(PMe_3)_2(CO)(X)$.

Complex	CO stretch (cm^{-1})	NO_x^- stretch (cm^{-1})
$Rh(PMe_3)_2(CO)(H)$	1978	—
$Rh(PMe_3)_2(CO)(CH_3)$	1959	—
$Rh(PMe_3)_2(CO)(NO_2)$	1987	1387, 1339
$Rh(PMe_3)_2(CO)(ONO)$	1976	1553, 1018
$Rh(PMe_3)_2(CO)(BMe_2)$	1958	—
$Rh(PMe_3)_2(CO)(BF_2)$	1977	—

Neutral $Rh(PMe_3)_2(py)(X)$.

Analogous to the $[CpRu(PMe_3)(L)(X)]^{0/-}$ calculations, we also considered L=pyridine, once again hoping to avoid dominant back donation into the carbonyl ligand. A comparison of the relevant NO_x^- stretches when L=CO vs py is summarized below in Table S6. No notable back donation is observed in the neutral case. In this case, we only focused on the nitrogen oxyanions to compare pyridine vs CO. Similar to the Ru case, the higher energy stretch features less mixing of vibrational motions, and therefore Table 6 only compares the higher energy stretch. The nitrate stretch for $Rh(PMe_3)_2(py)(ONO_2)$ is listed, but since the $Rh(PMe_3)_2(CO)(ONO_2)$ analogue did not optimize to a minimum, a comparison cannot be drawn.

Table S6. Comparison of NO_x^- stretches in $Rh(PMe_3)_2(L)(X)$ between L = py and CO.

Complex	NO_x^- stretch (cm^{-1}), L = py	NO_x^- stretch (cm^{-1}), L = CO	$\Delta = \nu(py) - \nu(CO)$
$Rh(PMe_3)_2(py)(ONO_2)$	1508	—	—
$Rh(PMe_3)_2(py)(NO_2)$	1380	1387	-7
$Rh(PMe_3)_2(py)(ONO)$	1525	1553	-28

One electron reduced $[Rh(PMe_3)_2(CO)(X)]^{0/-}$ calculations.

All species described above were reduced by 1 electron, analogous to the approach described with the $CpRu(PMe_3)(L)(X)$ system. A comparative list of stretching frequencies is detailed in Table S7. Again, because of the failure of $Rh(PMe_3)_2(CO)(ONO_2)$ to optimize, no comparison can be drawn for $[Rh(PMe_3)_2(CO)(ONO_2)]^-$. Table S8 similarly compares the neutral vs reduced pyridine calculations

Table S7. Calculated stretching frequencies for $[Rh(PMe_3)_2(CO)(X)]^-$. The CO stretches for the neutral species are shown in Table S5.

Complex	ν_{CO} (cm^{-1})	Δ(CO), anion - neutral	ν_{NO} (cm^{-1})	Δ(NO)
$[Rh(PMe_3)_2(CO)(H)]^-$	1840	-138	—	—
$[Rh(PMe_3)_2(CO)(CH_3)]^-$	1824	-135	—	—
$[Rh(PMe_3)_2(CO)(ONO_2)]^-$	1840	—	1398	—
$[Rh(PMe_3)_2(CO)(NO_2)]^-$	1831	-156	1321	-66
$[Rh(PMe_3)_2(CO)(ONO)]^-$	1829	-147	1442	-111
$[Rh(PMe_3)_2(CO)(BMe_2)]^-$	1832	-126	—	—
$[Rh(PMe_3)_2(CO)(BF_2)]^-$	1840	-137	—	—

Table S8. comparison of stretching frequencies for $[Rh(PMe_3)_2(py)(X)]^{0/-}$

Complex	ν_{NO} for neutral	ν_{NO} for anion	Δ, anion-neutral
$[Rh(PMe_3)_2(py)(ONO_2)]^{0/-}$	1508	1467	-41
$Rh(PMe_3)_2(py)(NO_2)^{0/-}$	1380	1331	-49
$Rh(PMe_3)_2(py)(ONO)^{0/-}$	1525	1466	-59

Upon one electron reduction, the highest energy ν_{NO} within all nitrogen oxyanions decreases (Table S8) which reflects increased back donation into NO_x; the vibrational mode shown is established as purely stretching of the terminal oxygen to nitrogen bonds. [The low energy stretch within the oxyanions is often strongly mixed with M/O stretching motion, which complicates interpretation of the shift of that observed frequency upon reduction; while the NO bond may weaken on reduction, the MO bond strengthens. For N-bound nitro this is not the case, and both N-O stretches decrease significantly when adding an electron to the system, consistent with the π-acidity of N-bound nitro. These values (Table S8) show considerable back donation in this trans planar structure for all *three* NO_x^-, which contradicts our conclusions on $CpRu(PMe_3)L$.

The spin density plots for the nitrogen oxyanion-containing species are shown in Figure S17 and S18. Figure S18 shows a spin density map of three of these complexes where X = NO_2^- and NO_3^-, and immediately reveals that the electron has not occupied a mainly metal orbital, but the spin density is overwhelmingly on the pyridine. Apparently the $\pi*$ orbital of pyridine in the neutral complex lies below its x^2-y^2 orbital, and thus reduction occurs primarily in the pyridine π system as found above with ruthenium (Figure ?). Consistent with reduced pyridine is the fact that, unlike the CO analog, the radical anion here does not yield a nonplanar coordination geometry around rhodium.

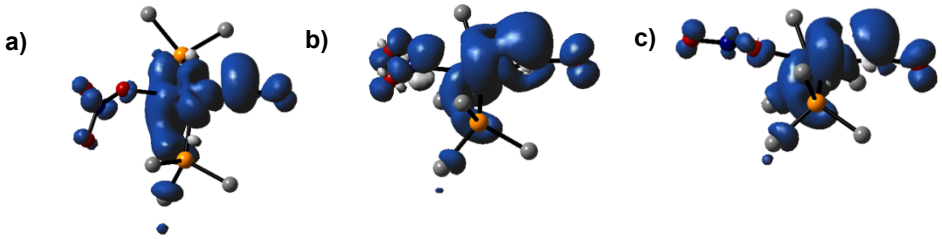

Figure S17. Spin density plots (0.002 au) for **a)** $[Rh(PMe_3)_2(CO)(ONO_2)]^-$ **b)** $[Rh(PMe_3)_2(CO)(NO_2)]^-$ **c)** $[Rh(PMe_3)_2(CO)(ONO)]^-$.

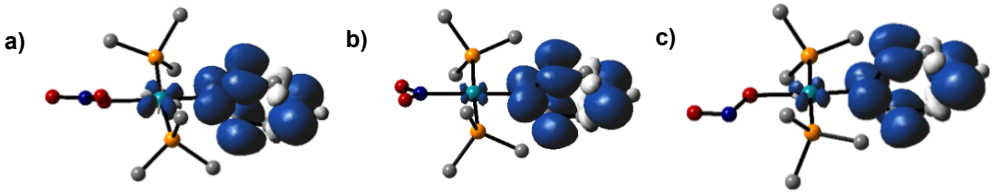

Figure S18. Spin density plots (0.002 au) for **a)** $[Rh(PMe_3)_2(pyr)(ONO_2)]^-$ **b)** $[Rh(PMe_3)_2(pyr)(NO_2)]^-$ **c)** $[Rh(PMe_3)_2(pyr)(ONO)]^-$.

Structural trends for $[Rh(PMe_3)_2(CO)(X)]^{0/-}$.

Geometry optimized structures show additional complexity (Figs S19-S28). In general, one electron reduction shortens the Rh-CO distance and lengthens the CO distance; the Rh-B distance also shortens, consistent with boryl π acid character, but the Rh-B distances never get as short as the Rh-CO distances. RhCO bending is much less than for the Ru examples, and in general it appears that unsaturation here leads to less transfer of electrons to the ligands than in the Ru examples. Dissociation of anionic NO_x^- ligand has progressed less than in nitrato and nitrito ruthenium cases, but is more advanced here for nitrate than nitrito. For $Rh(PMe_3)_2(CO)(X)$, the spectroscopic trends are significantly perturbed by large nonplanar structural variations,

mainly in the radical anions, enabled by lower coordination number here; in the neutral species, this could be due to trans influence between X and CO. These distortions from planarity reflect the change in the potential energy surface in going from d^8 one step towards the preferred tetrahedral of d^{10}. The angular distortions (both ∠PRhP and ∠LRhX) also destroy the rigorous symmetry-based σ/π separation, and metal orbitals mix more. Comparing the effect of reduction for BR_2 to NO_2, the former shows more angular distortion and Rh-B shortens but Rh-NO_2 *lengthens*. For neutral $Rh(PMe_3)_2(CO)(X)$, X = NO_2 and ONO have the two shortest Rh-C, consistent with weak binding of these X to Rh. However, on reduction, both BF and NO bonds (nitro isomer) lengthen, consistent with increased occupation of those X π* orbitals.

In contrast to $Rh(PMe_3)_2(CO)(X)$, all six $Rh(PMe_3)_2(py)(NO_x)$ are accurately planar at Rh. Bond lengths (CC and CN) show reduction of pyridine only in the anions, and the most N-oxyanion-dependent changes involve pyramidality of the pyridine nitrogen in the anions: angle $RhNC_{para}$ goes from 179.6° (NO_2) to 171.4° (ONO) to 163.8° (NO_3), an effect which could be interpreted as nitro *interacting strongest* with pyridine for the added electron. In $Rh(PMe_3)_2(py)(NO_2)^{-1\bullet}$ nitro is a competitive π acid. Flattening of pyridine anion nitrogen is best understood as a push/pull interaction of amidic reduced pyridine with all trans-positioned nitrogen oxyanions. Thus, compared to L = CO, π acidity of all NO_x^- can be manipulated by choice of ancillary ligands and stereochemistry. *Overall* these effects show that back donation is diminished in a 16 electron species vs. 18 electron, but that the pyridine LUMO is a strong competitor for back donation in all the species studied here. In contrast to $CpRu(PMe_3)L$ analogs, there is only marginal (< 0.04 Å) evidence for any NO_x^- dissociating from Rh in $Rh(PMe_3)_2(py)(NO_x)^{-1\bullet}$.

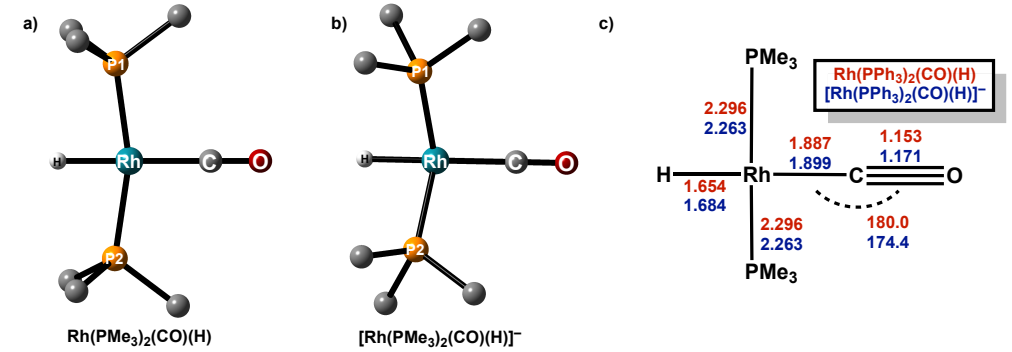

Figure S19. a) geometry optimized structure of $Rh(PMe_3)_2(CO)(H)$. P1–Rh–P2 angle is 163.7°, H–Rh–C angle is 180.0°. **b)** geometry optimized structure of $[Rh(PMe_3)_2(CO)(H)]^-$. P1–Rh–P2 angle is 134.4°, H–Rh–C angle is 162.2°. **c)** bond length comparison between $[Rh(PMe_3)_2(CO)(H)]^{0/-}$.

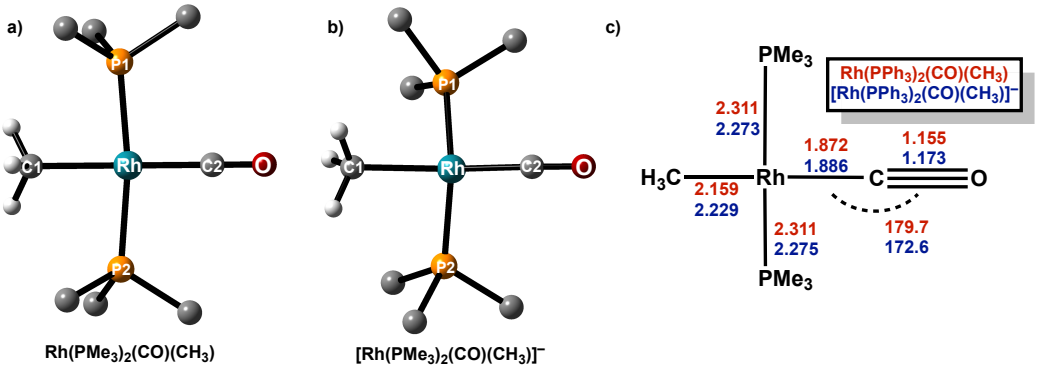

Figure S20. a) geometry optimized structure of $Rh(PMe_3)_2(CO)(CH_3)$. P1–Rh–P2 angle is 171.4°, C1–Rh–C2 angle is 179.2°. **b)** geometry optimized structure of $[Rh(PMe_3)_2(CO)(CH_3)]^-$. P1–Rh–P2 angle is 131.8°, C1–Rh–C2 angle is 159.9°. **c)** bond length comparison between $[Rh(PMe_3)_2(CO)(CH_3)]^{0/-}$.

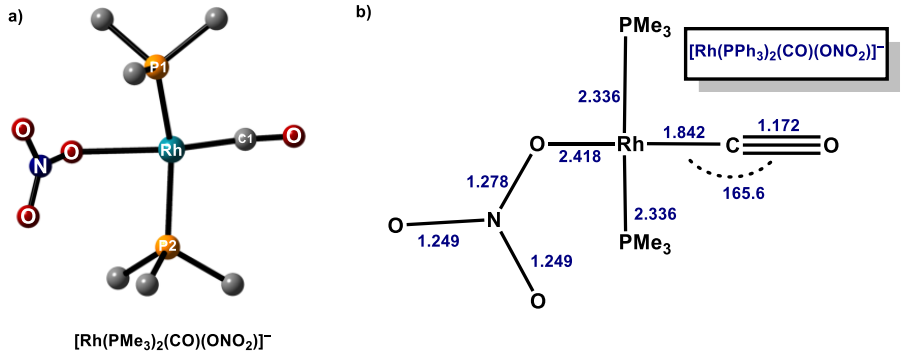

Figure S21. a) structure of $Rh(PMe_3)_2(CO)(\kappa^1\text{-}ONO_2)$ **b)** bond lengths in $Rh(PMe_3)_2(CO)(\kappa^1\text{-}ONO_2)$.

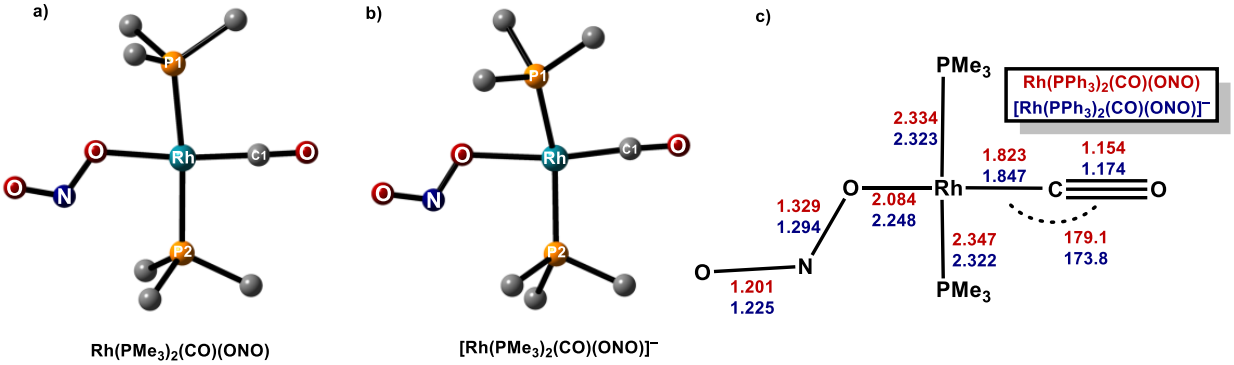

Figure S22. a) geometry optimized structure of $Rh(PMe_3)_2(CO)(\kappa^1\text{-}ONO)$ **b)** geometry optimized structure of $[Rh(PMe_3)_2(CO)(\kappa^1\text{-}ONO)]^-$. **c)** bond length comparison between $[Rh(PMe_3)_2(CO)(\kappa^1\text{-}ONO)]^{0/-}$.

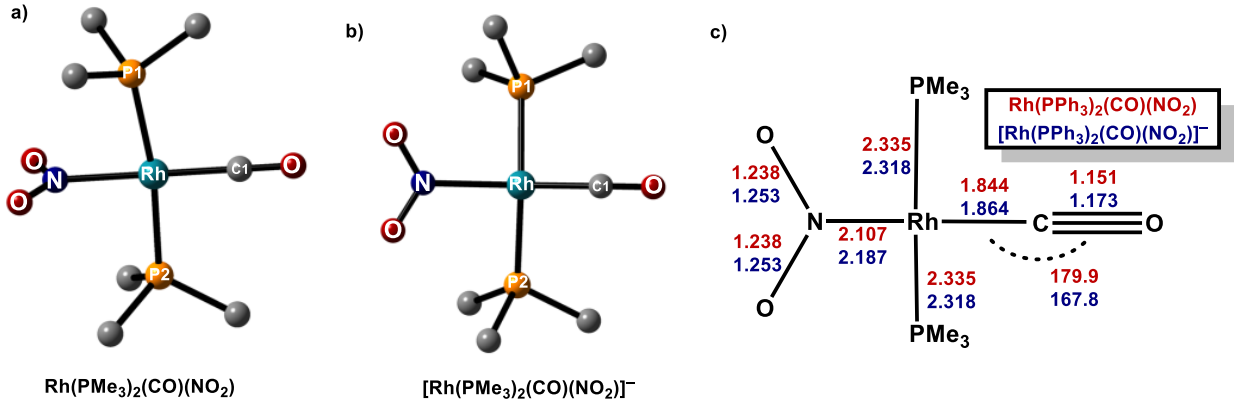

Figure S23. a) geometry optimized structure of $Rh(PMe_3)_2(CO)(NO_2)$ **b)** geometry optimized structure of $[Rh(PMe_3)_2(CO)(NO_2)]^-$. **c)** bond length comparison between $[Rh(PMe_3)_2(CO)(NO_2)]^{0/-}$.

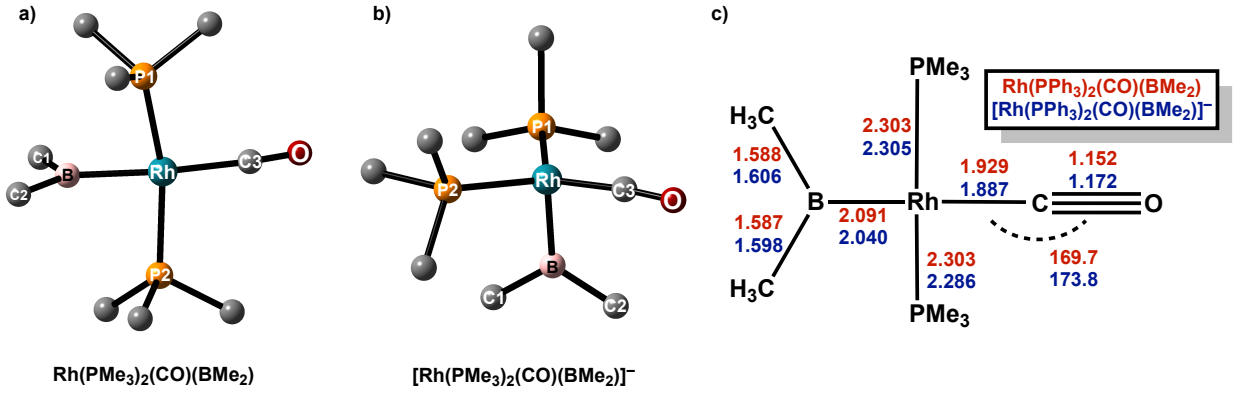

Figure S24. a) geometry optimized structure of $Rh(PMe_3)_2(CO)(BMe_2)$. P1–Rh–P2 angle is 161.8°, B–Rh–C3 angle is 166.0°. **b)** geometry optimized structure of $[Rh(PMe_3)_2(CO)(BMe_2)]^-$. P1–Rh–P2 angle is 110.6°, B–Rh–C3 angle is 94.1°, P2–Rh–C3 angle is 92.6°, P1–Rh–C3 angle is 99.1°, C3–Rh–P angles are between 121-125°. **c)** bond length comparison between $[Rh(PMe_3)_2(CO)(BMe_2)]^{0/-}$.

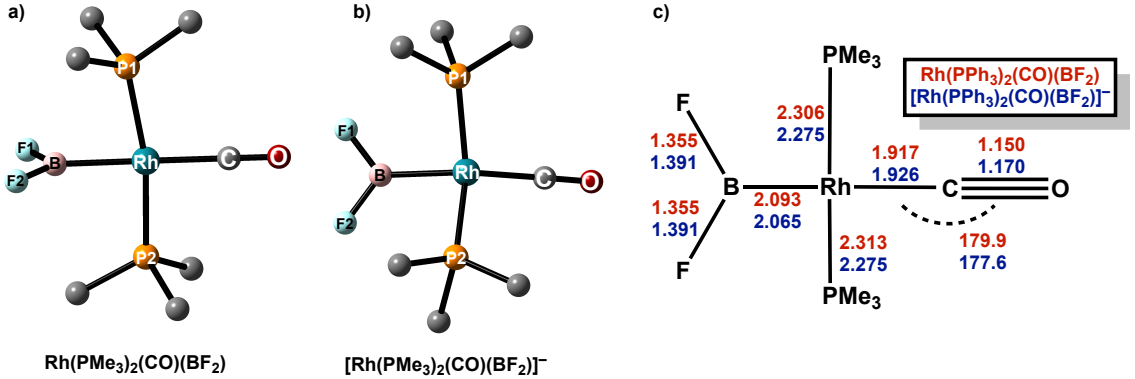

Figure S25. a) geometry optimized structure of $Rh(PMe_3)_2(CO)(BF_2)$. P1–Rh–P2 angle is 169.3°, B–Rh–C angle is 179.7°. **b)** geometry optimized structure of $[Rh(PMe_3)_2(CO)(BF_2)]^-$. P1–Rh–P2 angle is 143.0°, B–Rh–C angle is 147.8°. **c)** bond length comparison between $[Rh(PMe_3)_2(CO)(BF_2)]^{0/-}$.

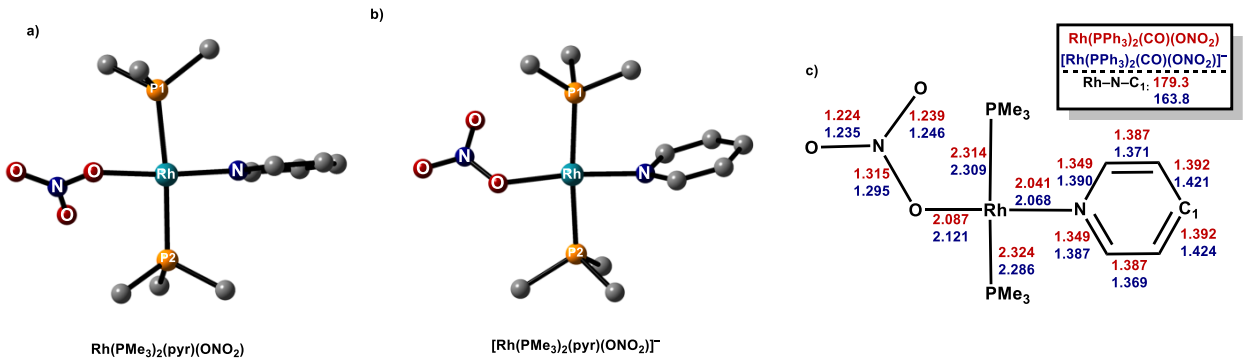

Figure S26. a) structure of $Rh(PMe_3)_2(py)(ONO_2)$ **b)** structure of $[Rh(PMe_3)_2(py)(ONO_2)]^-$ **c)** bond length comparison between $[Rh(PMe_3)_2(py)(ONO_2)]^{0/-}$.

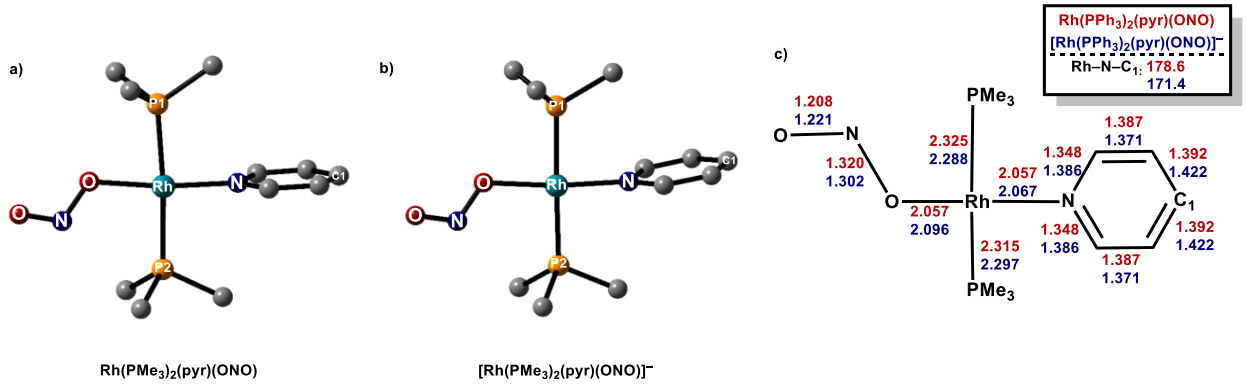

Figure S27. a) geometry optimized structure of $Rh(PMe_3)_2(py)(\kappa^1\text{-}ONO)$ **b)** geometry optimized structure of $[Rh(PMe_3)_2(py)(\kappa^1\text{-}ONO)]^-$. **c)** bond length comparison between $[Rh(PMe_3)_2(py)(\kappa^1\text{-}ONO)]^{0/-}$.

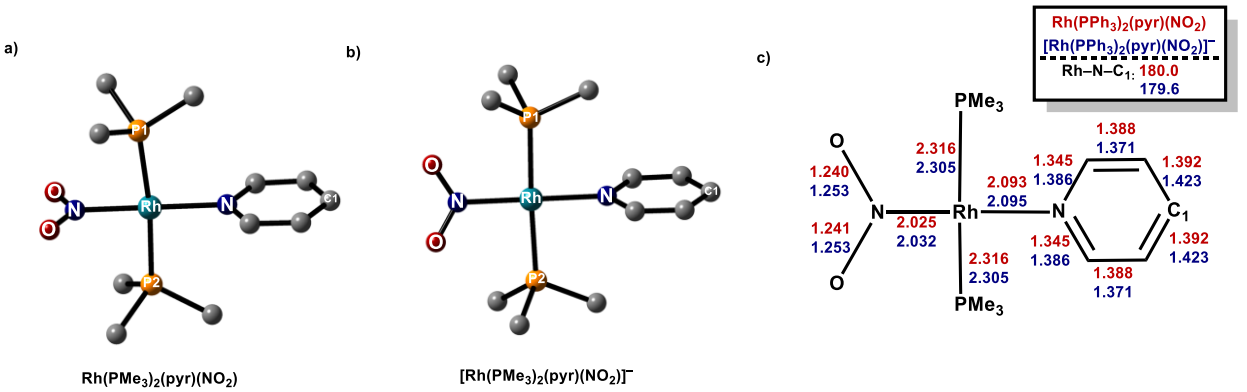

Figure S28. a) geometry optimized structure of $Rh(PMe_3)_2(CO)(NO_2)$ **b)** geometry optimized structure of $[Rh(PMe_3)_2(CO)(NO_2)]^-$. **c)** bond length comparison between $[Rh(PMe_3)_2(CO)(NO_2)]^{0/-}$.

$[Rh(PMe_3)_2(L)(X)]^{0/-}$ conclusions.

Overall, these calculations mirror those seen in the $[CpRu(PMe_3)(L)(X)]^{0/-}$. Spin density in all reduced complexes locates primarily on metal or CO, even pyridine. Only small bond length changes within the M-X unit were observed. This, in conjunction with coupled stretching frequencies between nitrogen oxyanions and ancillary ligand motions makes this particular set of compounds insufficient for our overall goal of identifying specific design principles for nitrogen oxyanion bond weakening.

Supplementary discussion of $[(TCB)Ru(NO_x)]^{0/-}$ calculations.

Free nitrate dianion.

Because of the pyramidalization of nitrate observed in the case of $[(TCB)Ru(\kappa^2\text{-}NO_3)]^-$, calculations on the free nitrate dianion were performed. The optimized structure is pyramidal at nitrogen (sum of N-O angles = 349.9°) and the nitrogen lies 0.25 Å out of the O_3 plane (Figure S29). The dianion is C_{3v} symmetric, and each N-O bond is lengthened by 0.1 Å with respect to the monoanion. The spin density of the dianion shows delocalization throughout the π system, with the largest contribution on nitrogen (Figure S29). Furthermore, the calculated N-O stretching frequency decreases by 373 cm^{-1} upon reduction of nitrate – all of these factors support the assignment of $[(TCB)Ru(\kappa^2\text{-}NO_3^{2-})]^-$.

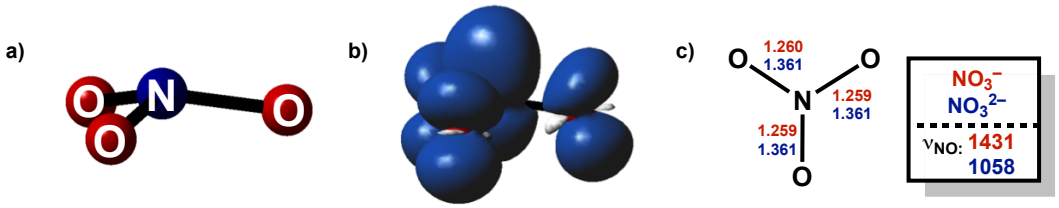

Figure S29. a) optimized structure of NO_3^{2-}. **b)** Spin density plot (0.002 au) of NO_3^{2-}. **c)** comparison of NO_3^{2-} to NO_3^{-}.

Monodentate NO_x^- with TCB.

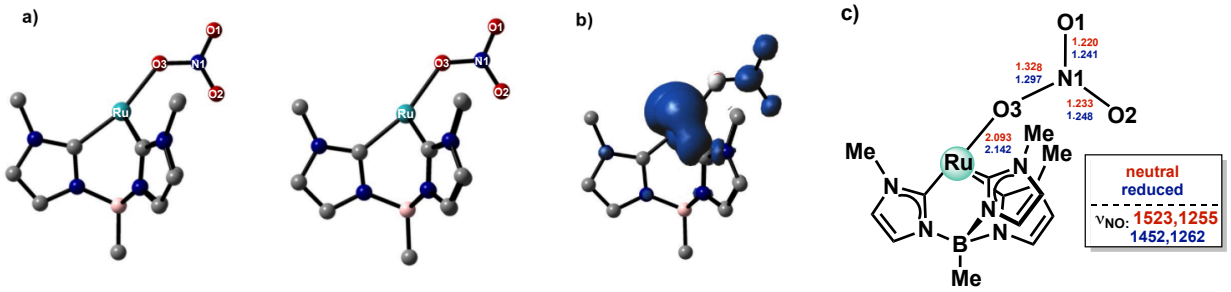

Figure S30. a) optimized structures of $[(TCB)Ru(\kappa^1\text{-}NO_3)]^{0/-}$ **b)** Spin density plot (0.002 au) of $[(TCB)Ru(\kappa^1\text{-}NO_3)]^-$ **c)** structural comparison of $[(TCB)Ru(\kappa^1\text{-}NO_3)]^{0/-}$.

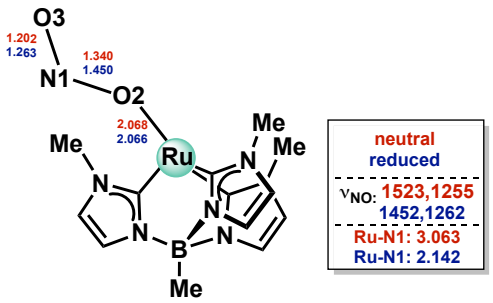

Figure S31. Structural comparison of $[(TCB)Ru(\kappa^1\text{-}ONO)]^{0/-}$.

A deviation from co-planarity of the R-N=O species with the metal seems to be directly correlated to R-N=O reduction, which is evidenced based on N=O bond lengths in Table S9. The N-O distance is elongated from a true double bond in nitrosobenzene in the structures that are non-coplanar with the metal. Importantly, the charge assigned to the metal in Table S9 only takes into account ancillary ligands and thus considers R-N=O to be neutral, regardless of N=O bond length. This charge assignment is useful in qualitatively understanding the reducing power of each metal towards neutral R-N=O. Thus, for entries 1 and 2, Pd and Pt 0 are quite reducing, and give long N=O distances in the R-N=O fragment, ultimately indicating reduction at the R-N=O ligand and oxidation of the metal center. Notably, in the case of the Mn(0) (entry RUSZUC) which we would expect to reduce R-N=O, the co-planarity is most likely sterically enforced.

Single and two-electron reduction of R-N=O has been addressed comprehensively for RNO, and can be equally well applied to nitrite radical dianion, upon reduction of NO_2^{1-}. What was not recognized was the nonplanarity of MNO and the R atom bound to N in *certain* compounds, specifically those with long NO bonds, hence reduced cases (Table S9). Shown in Scheme S1 are Lewis structures for both, emphasizing that reduction converts nitrogen from sp^2 to sp^3 hybridization. Although one of the orbitals on nitrogen is only singly occupied, this hybridization

change moves the pendant oxo group out of the MNO plane (M, not shown, lies in the plane of the page). The relationship to RNO is best seen by placing an electrophile R on the pendant nitro oxygen (Scheme S1). An additional consequence of reduction is a lengthening of the NO bond, seen dramatically in organonitroso compounds, from 1.24 to 1.35 and finally to 1.42 Å, and the simple Lewis structure picture also accounts for that. In summary, just as in the nitrate radical dianion, hybridization change to accommodate an added electron gives pyramidality as a diagnostic of nitro group reduction.

Table S9. Cambridge Database REFcodes of κ^2-M[RNO] structures showing correlation of N-O bond lengthening (green and yellow) with pyramidalization at N.

Refcode	Metal	Charge	MNOR planar?	N=O distance (Å)	Reference
AGUJUJ	Pd	0	no	1.349	[1]
FOHTOL	Pt	0	no	1.410	[2]
GEWPOQ	Cu	+1	yes	1.236	[3]
GEWPUW	Cu	+1	yes	1.264	[3]
GEWQAD	Cu	+1	yes	1.266	[3]
IMOJOK	Mo	+4	no	1.417	[4]
IMOJUQ	W	+4	no	1.447	[4]
IWOVUN	Ni	+1	yes	1.323	[5]
LUTQUN	Cu	+1	no	1.333	[6]
LUTRAU	Cu	+1	no	1.335	[6]
OZUREI	Cu	+1	yes	1.25	[7]
PIXKEM	W	+4	no	1.431	[8]
POLWEV	Co	0	no	1.366	[9]
RUSZUC	Mn	0	yes	1.264	[10]
SOYYAJ	Co	+1	no	1.371	[11]
YIDTAG	Ru	0	no	1.412	[12]

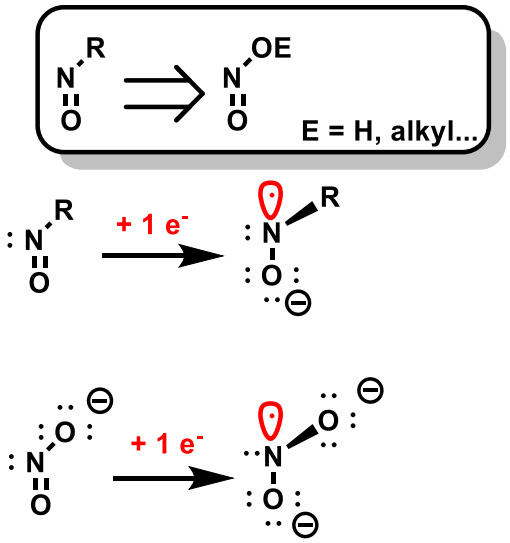

Scheme S1. Pyramidalization of nitrogen at RNO and NO_2^- upon 1 electron reduction.

Solvation calculation comparison for protonation calculations.

To consider the different possible effects of solvent, we took the optimized geometries of the compounds shown in Scheme 1 and performed single point energy calculations with solvents of varied dielectric constants: benzene, THF, and acetonitrile.

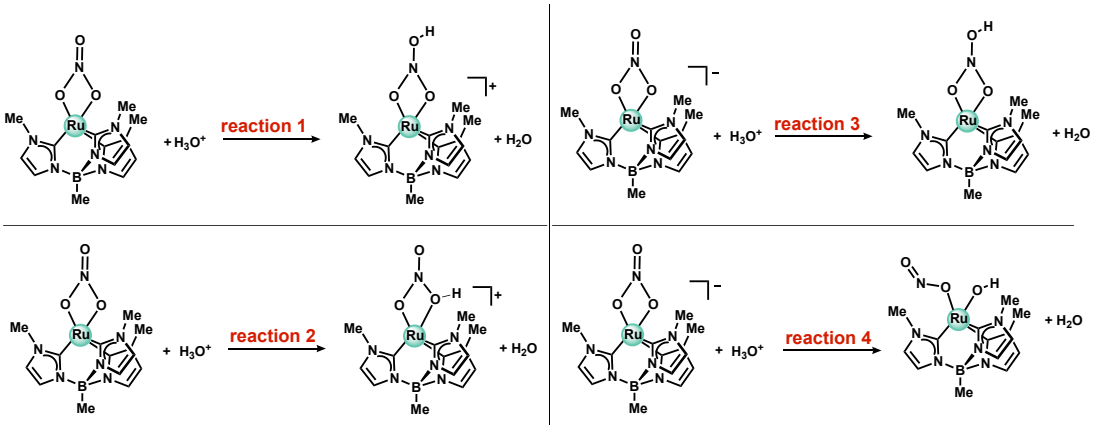

Scheme S2. Schemes showing labelling used for Table S10

Table S10. Comparison of thermodynamics for protonation reactions (in kcal/mol) for varied implicit solvent corrections

	No solvent corrections	benzene	THF	acetonitrile
Reaction 1	-46.0	-22.5	-11.4	-8.5
Reaction 2	-44.9	-21.7	-10.8	-8.1
Reaction 3	-163.2	-96.3	-59.7	-46.6
Reaction 4	-203.2	-137.9	-102.9	-90.3

For reactions 3 and 4, we found that as the dielectric constant increases, the thermodynamic favorability of the reaction decreases (although in every case they're still incredibly exergonic). This is because in reactions 3 and 4 the reactants are charged species and the products are uncharged. So the reactants are stabilized by more polar solvents, making the overall process less favorable. With nonpolar solvents like benzene there is not a significant amount of stabilization of charged species. For reactions 1 and 2 however, the charges are equal on the product and reactant side, which might lead us to believe that the solvent corrections would have a lesser effect, however we still find a considerable change with solvent corrections included. We attribute this to the general size of the cation on products vs reactants side: a small H_3O^+ compared to the charged ruthenium complex. Overall, this demonstrates that all reactions are still downhill, but solvent corrections are important to include when considering this thermodynamic data.

Protonation of [(TCB)Ru(κ^2-NO$_3$)]$^{0/-}$.

To help confirm the assignment of +3 oxidation state in the N/O bond scission product (TCB)Ru(κ^1-ONO)(OH) that resulted from protonation of (TCB)Ru(κ^2-NO$_3$) we visualized the spin density plot as well as the SOMO of the (TCB)Ru(κ^1-ONO)(OH) product (Figure S32)

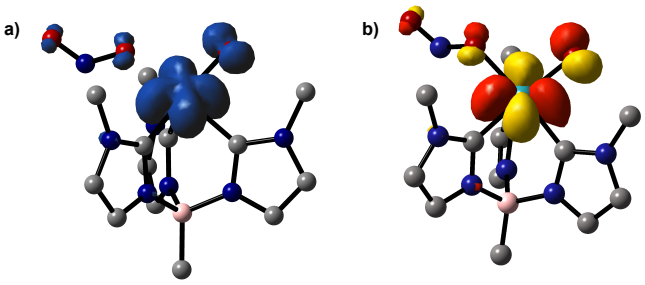

Figure S32. a) spin density plot (0.002 au) and b) SOMO (0.05 au) of (TCB)Ru(κ^1-ONO)(OH)

Both the spin density plot and the SOMO help confirm the Ru(III) assignment, showing the unpaired electron resides primarily on the Ru center, with minor contributions on the hydroxide and nitrite ligands and no significant character on the TCB ligand. The electron resides in the dxy orbital, consistent with 1 electron oxidation of Ru in the qualitative MO diagram depicted in the manuscript (Figure 8d)

Protonation of [(TCB)Ru(nitrite)]$^{0/-}$.

Not only is nitrite more complex because of the two isomers, but breaking an N-O bond after protonation of [(TCB)Ru(κ^2–ONO)]$^-$ would necessitate the formation of an isonitrosyl ligand. O-protonation of neutral (TCB)Ru(κ^2–ONO) to form [(TCB)Ru(ONOH)]$^+$ causes (Figure S33) bidentate nitrite to become essentially monodentate, with the protonated Ru-O distance elongating by 0.54 Å. To compensate for the lost donation from the protonated oxygen, the other Ru-O distance shortens by 0.1 Å. The N-OH bond is lengthened by 0.14 Å, consistent with the loss of double bond character. As with other four coordinate (TCB)Ru complexes, the geometry is best described as see-saw, with a nearly linear O-Ru-C angle of 177.4°. In contrast, the protonation of [(TCB)Ru(κ^2–ONO)]$^-$ to form neutral (TCB)Ru(ONOH) results in barrierless N-O bond scission to form (TCB)Ru(OH)(ON) (Figure S34), where the formation of an isonitrosyl is *not* an impediment to bond cleavage.

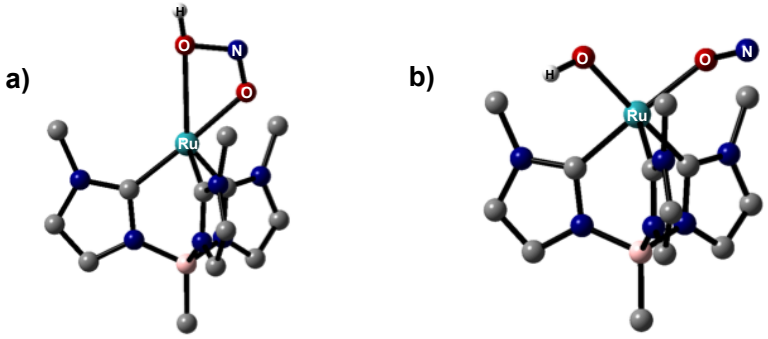

Figure S33. a) optimized structures for [(TCB)Ru(ONOH)]$^+$ and **b)** (TCB)Ru(OH)(ON).

The anion [(TCB)Ru(κ^2-ONO)]$^-$ thus has enough reducing power to undergo the two electron process of breaking an N-O bond, certainly facilitated by the large amount of spin density on the nitrito ligand in [(TCB)Ru(κ^2–ONO)]$^-$. Similarly to the protonation of the internal oxygen of [(TCB)Ru(O_2NO)]$^-$, this bond cleavage is enabled by the preformed M-O bond of the hydroxide ligand, thus the connectivity of (TCB)Ru(OH)(ON) is already in place before bond scission. The isonitrosyl ligand could isomerize to nitrosyl or even liberate free NO; however, neither of these processes is barrierless and thus the isonitrosyl is found as a local minimum.

Protonation of neutral (TCB)Ru(NO_2) results in a shortening of the Ru-N bond by 0.043 Å, a result of the short Ru-O contact being lost after O-protonation. Protonation increases the Ru-N-O angle by 20°. The geometry in [(TCB)Ru(N(OH)O)]$^+$ is see-saw (Figure S34), with an N-Ru-C angle of 179.9°. Protonation of [(TCB)Ru(NO_2)]$^-$ gives again barrierless cleavage to a structure that is a minimum, showing Ru(III) and a nitrosyl and hydroxide ligand (Figure S34).

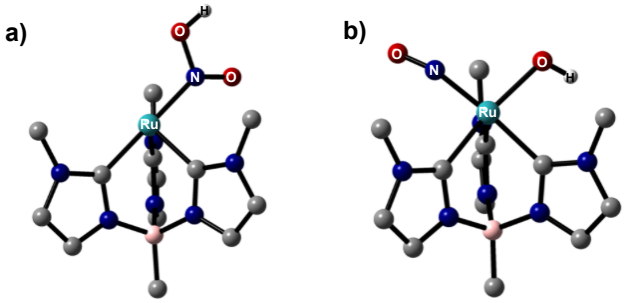

Figure S34. a) optimized structures for $[(TCB)Ru(N(OH)O)]^+$ and **b)** (TCB)Ru(OH)(NO).

Overall, these results mirror the nitrate protonation conclusion, and indicate that when significant spin density is on either oxyanion, protonation leads to N-O bond scission and formation of a hydroxide ligand coordinated to Ru^{III}.

Alkali metal assist of N/O bond cleavage?

With protonation inducing N/O bond cleavage of nitrate and nitrite, we sought to learn whether an alkali metal could facilitate the same transformation. To be realistic, the sodium cation was coordinated by 1,2-dimethoxyethane (DME). Calculations on (TCB)Ru(κ^2–NO_3)Na(DME) and $[(TCB)Ru(\kappa^2–NO_3)Na(DME)]^+$ were done analogously to the nitrate protonation calculations. $[(TCB)Ru(\kappa^2–NO_3)Na(DME)]^+$ with Na^+ on one internal oxygen shows only minor structural changes with respect to (TCB)Ru(κ^2–NO_3). The C_{2v} symmetry of nitrate is broken, with the oxygen interacting with the sodium having a shorter Ru-O distance by 0.096 Å. The geometry about ruthenium is unaltered at square pyramidal. Reduction of this species by one electron to give (TCB)Ru(κ^2–NO_3)Na(DME) reveals that N/O bond scission has progressed, evidenced by a 0.13 Å increase in the N-ONa distance, but has not broken. This bond lengthening is accompanied by a 0.097 Å shortening of the Ru-ONa distance. This (TCB)Ru(κ^2–NO_3)Na(DME) has pyramidal nitrate nitrogen, with lengthening of all N-O bonds, suggesting charge density located in the nitrate π^*. Alkali metalation of nitrate in $[(TCB)Ru(\kappa^2–NO_3)]^-$ shows no N/O bond scission, in contrast to protonation.

With Na^+ initially on the terminal oxygen in (TCB)Ru(κ^2–NO_3)Na(DME), the nitrate nitrogen is again pyramidal (Figure S35), and internal N-O bond distances differ by 0.084 Å. The C_{2v} symmetry of nitrate is lost, with one Ru-O distance shorter by 0.085 Å. These bond lengths indicate progress towards a ruthenium oxo and Ru-O-N=O-Na moiety; however, no spontaneous bond cleavage is observed. The Na^+ is *four* coordinate, interacting with two nitrate oxygens.

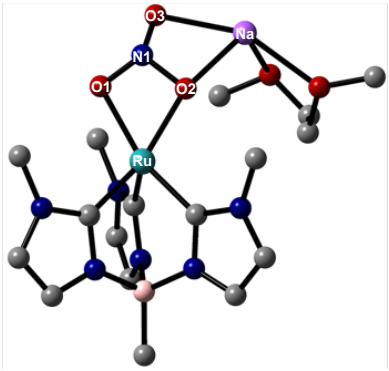

Figure S35. Geometry optimized structure of (TCB)Ru(κ^2–NO_3)Na(DME), showing Na^+ migrated to two nitrate O, but retention of all N/O bonds

Discussion of $[(Tp)Ru(NO_x)]^{0/-}$ calculations.

Nitrate results.

Because this work seeks to identify general design principles that affect NO_x^-, we wanted to probe how central the tris NHC ligand is to formation of the nitrate dianion. Geometry optimization of 16 valence electron $(Tp)Ru(\kappa^2\text{–}NO_3)$ (Tp = tris-pyrazolylborate) yields a square pyramidal structure similar to $(TCB)Ru(\kappa^2\text{–}NO_3)$; however, each Ru-O distance is *shortened* by 0.076 Å compared to the (TCB) complex, showing the influence of the strongly donating carbenes. The unpaired spin of the reduced $[(Tp)Ru(\kappa^2\text{–}NO_3)]^-$ is in primarily a ruthenium d-orbital, which is directed towards the vacant site of the square pyramid. This follows the generality that d^6 is square pyramidal and d^7 is the same, with its SOMO in the open coordination site. The spin density of $[TpRu(\kappa^2\text{–}NO_3)]^-$ has only minor nitrate contribution, and the bond length changes, as well as N-O stretching frequencies, are not consistent with back donation into the π-system of nitrate upon reduction. In fact, upon reduction, the Ru-O distances lengthen by 0.02 Å, while the internal N-O distances shorten by 0.007 Å and the terminal N-O distance lengthens by 0.022 Å. Furthermore, the higher energy NO stretching frequency decreases by only 73 cm^{-1} (Figure S36).

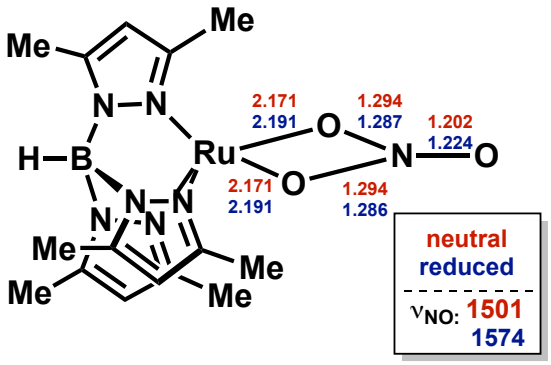

Figure S36. Structural comparison of $[(Tp)Ru(\kappa^2\text{–}NO_3)]^{0/-}$.

Nitrite results.

For comparison of NO_2^- to NO_3^-, calculations were also done on $(Tp)Ru(\kappa^2\text{–}ONO)$ and $[(Tp)Ru(\kappa^2\text{–}ONO)]^-$. Once again, the bidentate nitrite complex is square pyramidal about ruthenium (Figure S37). The spin density of monoanionic $[(Tp)Ru(\kappa^2\text{–}ONO)]^-$ (Figure S37) is mainly located in a metal orbital, once again directed towards the vacant site of the square pyramid. There is certainly some spin density on the nitrite ligand, and bond length changes as well as shift in the N-O stretching frequency (decreased by 32 cm^{-1}) are all consistent with back donation, but changes, upon reduction, are modest compared to those seen for the TCB analogue.

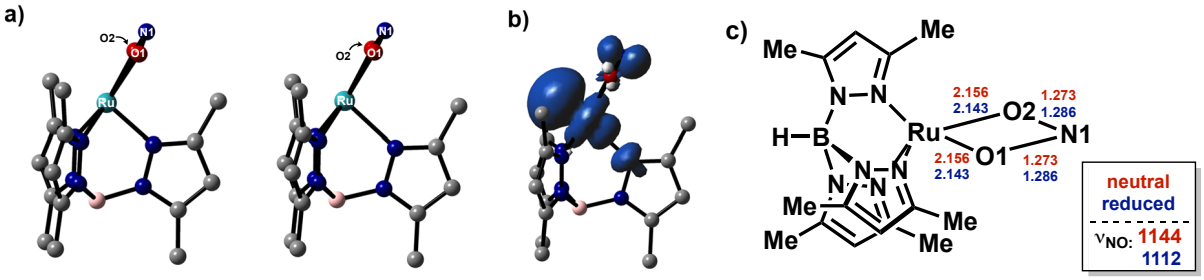

Figure S37. a) optimized structures of $[(Tp)Ru(\kappa^2\text{–}ONO)]^{0/-}$. **b)** Spin density plot (0.002 au) of $[(Tp)Ru(\kappa^2\text{–}ONO)]^-$ **c)** structural comparison between $[(Tp)Ru(\kappa^2\text{–}ONO)]^{0/-}$

Protonation of [(Tp)Ru(κ²–NO₃)]$^{0/-}$.

We were interested in whether we would observe N-O bond scission with the Tp ligand, as we did with the more strongly donating TCB ligand. The thermodynamics for protonation are shown in Scheme S3 and all optimized structures are shown in Figure S38. Overall, we see the same trend. These calculations were optimized in the gas phase, and the thermodynamic data is reported as such, however we predict that the same trends observed with solvent corrections for TCB would be observed for Tp.

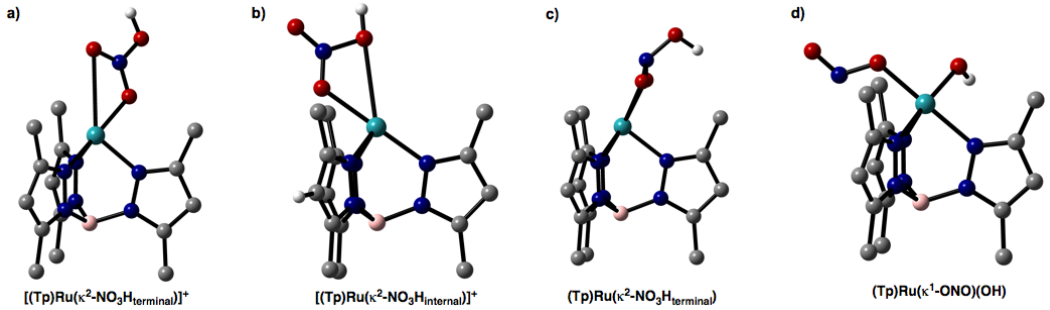

Figure S38: optimized structures of a) [(Tp)Ru(κ²-$NO_3H_{terminal}$)]$^+$ b) [(Tp)Ru(κ²-$NO_3H_{internall}$)]$^+$ c) (Tp)Ru(κ²-$NO_3H_{terminal}$) and d) (Tp)Ru(κ¹-ONO)(OH).

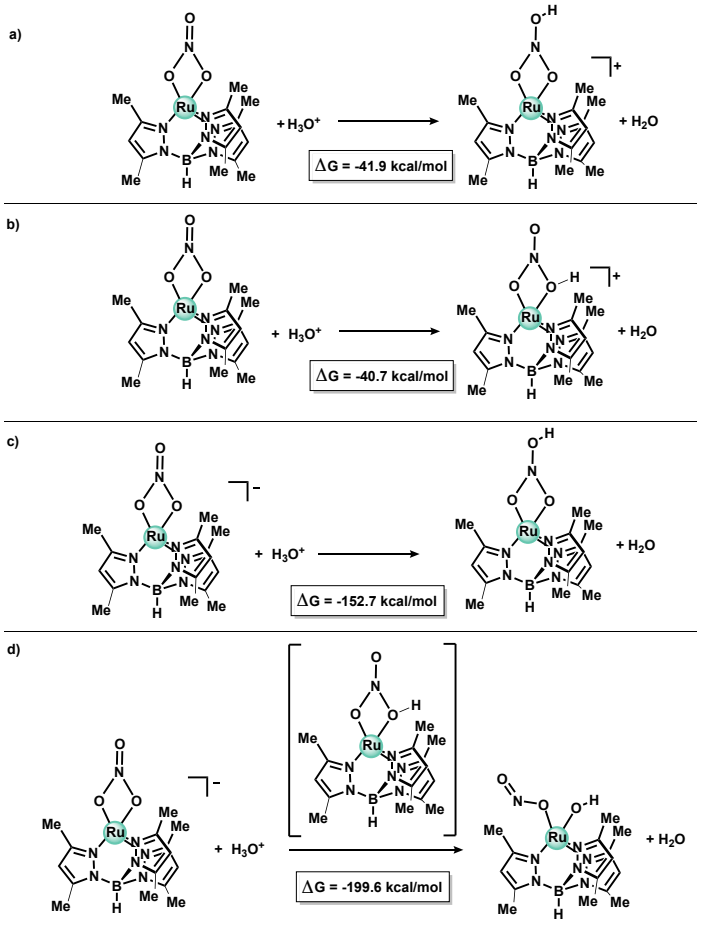

Scheme S3. Thermodynamics for N/O bond scission with Tp calculations

References.

1. B. R. Barnett, L. A. Labios, C. E. Moore, J. England, A. L. Rheingold, K. Wieghardt and J. S. Figueroa, *Inorg.Chem.*, 2015, **54**, 7110-7121.
2. M. Pizzotti, F. Porta, S. Cenini, F. Demartin and N. Masciocchi, *J. Organomet. Chem.*, 1987, **330**, 265-278.
3. F. Effaty, J. Zsombor-Pindera, A. Kazakova, B. Girard, M. S. Askari and X. Ottenwaelder, *New J. Chem.*, 2018, **42**, 7758-7764.
4. P. M. Graham, M. S. A. Buschhaus, R. A. Baillie, S. P. Semproni and P. Legzdins, *Organometallics*, 2010, **29**, 5068-5072.
5. S. Kundu, S. C. E. Stieber, M. G. Ferrier, S. A. Kozimor, J. A. Bertke and T. H. Warren, *Angew. Chem. Int. Ed.*, 2016, **55**, 10321-10325.
6. S. Wiese, P. Kapoor, K. D. Williams and T. H. Warren, *J. Am. Chem. Soc.*, 2009, **131**, 18105-18111.
7. K. D. Williams, A. J. P. Cardenas, J. D. Oliva and T. H. Warren, *Eur, J. Inorg. Chem.*, 2013, **2013**, 3812-3816.
8. E. B. Brouwer, P. Legzdins, S. J. Rettig and K. J. Ross, *Organometallics*, 1994, **13**, 2088-2091.
9. D. Wang, X. Leng, S. Ye and L. Deng, *J. Am. Chem. Soc.*, 2019, **141**, 7731-7735.
10. D. W. Agnew, C. E. Moore, A. L. Rheingold and J. S. Figueroa, *Angew. Chem. Int. Ed.*, 2015, **54**, 12673-12677.
11. C. C. Mokhtarzadeh, C. Chan, C. E. Moore, A. L. Rheingold and J. S. Figueroa, *J. Am. Chem. Soc.*, 2019, **141**, 15003-15007.
12. S. J. Skoog, J. P. Campbell and W. L. Gladfelter, *Organometallics*, 1994, **13**, 4137-4139.